CDKN2A^{Low} cancer cells outcompete macrophages for microenvironmental zinc to drive immunotherapy resistance

Raquel Buj[1], Aidan R. Cole[1], Jeff Danielson[1], Jimmy Xu[2], Drew Hurd[3], Akash Kishore[4], Katarzyna M. Kedziora[5], Jie Chen[3], Baixue Yang[1,6], David Barras[7], Apoorva Uboveja[1], Amandine Amalric[1], Juan J. Apiz Saab[8], Jayamanna Wickramasinghe[9], Naveen Kumar Tangudu[1], Evan Levasseur[1], Hui Wang[1], Aspram Minasyan[7], Rebekah E. Dadey[3], Allison C. Sharrow[1], Frank P. Vendetti[10], Dayana B. Rivadeneira[11], Christopher J. Bakkenist[1,10], Greg M. Delgoffe[11], Nadine Hempel[3], Nathaniel W. Snyder[12], Riyue Bao[3], Adam C. Soloff[13], John M. Kirkwood[3], Denarda Dangaj Laniti[7], Andrew V. Kossenkov[9], Alexander Muir[8], Jishnu Das[4], Diwakar Davar[3], Clementina Mesaros[2], Katherine M. Aird[1]*

[1]Department of Pharmacology & Chemical Biology and UPMC Hillman Cancer Center, University of Pittsburgh School of Medicine, Pittsburgh, PA

[2]Department of Pharmacology, University of Pennsylvania, Philadelphia, PA

[3]Department of Medicine and UPMC Hillman Cancer Center, University of Pittsburgh, Pittsburgh, PA

[4]Center for Systems Immunology, Departments of Immunology and Computational & Systems Biology, University of Pittsburgh School of Medicine, Pittsburgh, PA

[5]Department of Cell Biology, Center for Biologic Imaging, University of Pittsburgh School of Medicine, Pittsburgh, PA

[6]Tsinghua University School of Medicine, Beijing, P.R. China

[7]Ludwig Institute for Cancer Research, Lausanne Branch, University of Lausanne (UNIL), Department of Oncology, Lausanne University Hospital (CHUV) and University of Lausanne, and Agora Cancer Research Center, Lausanne, Switzerland

[8]Ben May Department for Cancer Research, University of Chicago, Chicago, IL, USA

[9]The Wistar Institute of Anatomy and Biology, Philadelphia, PA

[10]Department of Radiation Oncology and UPMC Hillman Cancer Center, University of Pittsburgh School of Medicine, Pittsburgh, Pennsylvania, PA

[11]Department of Immunology and UPMC Hillman Cancer Center, University of Pittsburgh School of Medicine, Pittsburgh, PA

[12]Aging + Cardiovascular Discovery Center, Department of Cardiovascular Sciences, Lewis Katz School of Medicine, Temple University, Philadelphia, PA

[13]Department of Cardiothoracic Surgery and UPMC Hillman Cancer Center, University of Pittsburgh School of Medicine, Pittsburgh, PA

*Corresponding Author
Katherine M. Aird, PhD
Associate Professor
5051 Centre Ave.
Office: 2041; Lab 2050
Pittsburgh, PA 15213
412-648-4823
Katherine.aird@pitt.edu

Running title: Zinc modulates immunotherapy response in *CDKN2A*^{Low} tumors

Keywords: SLC39A9**,** ZIP9, tumor microenvironment (TME), phagocytosis, p16, anti-PD1, anti-PD-L1, immune checkpoint blockade (ICB), tumor interstitial fluid (TIF), dietary intervention, zinc, metabolism, metals

ABSTRACT

Approximately 50% of cancers exhibit decreased *CDKN2A* expression (*CDKN2A*^{Low}), which is linked to immune checkpoint blockade (ICB) resistance. While *CDKN2A* is traditionally recognized as a tumor suppressor and cell cycle regulator, we have previously put forth a new paradigm demonstrating its role in intracellular metabolic reprogramming. Whether the metabolic derangement due to *CDKN2A* loss alters metabolites within the tumor microenvironment (TME) and how that affects the immune compartment and ICB response has never been investigated. Here we found that *CDKN2A*^{Low} cancer cells reorganize zinc compartmentalization by upregulating the zinc importer SLC39A9 in the plasma membrane, leading to intracellular zinc accumulation in cancer cells and concurrent zinc depletion in the TME. This competition for zinc results in zinc-starved macrophages, leading to reduced phagocytic activity. Remarkably, restoring zinc levels in the TME through a dietary intervention re-educates macrophages to a pro-phagocytic phenotype, sensitizing *CDKN2A*^{Low} tumors to ICB. Unexpectedly, T cells are not required for this response. Clinically, macrophages from *CDKN2A*^{Low} cancer patients have decreased zinc signatures, corresponding to reduced phagocytosis signatures. Moreover, patients with low circulating zinc levels have reduced time-to-event outcomes compared to those with higher zinc levels. Our work reveals a previously unrecognized mechanism through which *CDKN2A*^{Low} cancer cells outcompete macrophages for zinc, directly disrupting their function and ICB efficacy.

INTRODUCTION

The Cyclin-Dependent Kinase Inhibitor 2A (*CDKN2A*) gene, located on chromosome 9p21, is a critical tumor suppressor and one of the most frequently altered loci in human cancers, with disruptive alterations observed in approximately 50% of all cases[1,2]. *CDKN2A* encodes two distinct proteins through alternative reading frames: $p14^{ARF}$ ($p19^{ARF}$ in mice) and $p16^{INK4A}$ (hereafter p16), both of which are essential regulators of the cell cycle[3]. While canonical roles of *CDKN2A* in cell cycle regulation and senescent induction is well established, evidence from our laboratory and others suggests that its functions extend beyond this paradigm[4-15]. We have demonstrated that loss of *CDKN2A*/p16 expression reprograms intracellular metabolism, enhancing key biosynthetic metabolites that contribute to cellular proliferation and tumorigenesis, including nucleotides and cholesterol[4,7]. However, whether this metabolic disruption downstream *CDKN2A* loss affects the metabolic landscape of the tumor microenvironment (TME) remains unexplored.

A number of data mining studies have highlighted a significant correlation between *CDKN2A* genetic alterations and a pro-tumorigenic TME, as well as poor response to immune checkpoint blockade (ICB) therapies[5,16-32]. ICB therapies, particularly monoclonal antibodies targeting the PD-1/PD-L1 axis, have become a cornerstone in cancer treatment, demonstrating significant clinical success across several cancers[33-37]. Their effectiveness is primarily attributed to enhancing T cell activity and T cell-mediated tumor killing[38]. However, PD-1 has been found to be expressed in a variety of cell types, including tumor-associated macrophages (TAMs)[39-42], suggesting that these cells may also

influence the efficacy of ICB therapies. In this regard, recent evidence suggests that at least a subset of TAMs play a role in the response to ICB[39,42-48]. Anti-PD-1/PD-L1 therapies directly target monocytes and macrophages to improve therapeutic responses at least in part via increasing their phagocytic activity[39,42,49,50]. Indeed, studies have shown that increased TAM phagocytic activity inhibits tumor growth in mouse models[51-53]. While metabolic reprogramming is known to influence macrophage phagocytic activity[51,54,55], the role of cancer-TAM nutrient competition in driving this process remains poorly understood.

Zinc is an essential trace element and the second most abundant metal in the human body[56]. Zinc is primarily obtained through the diet and absorbed in the intestine from where it is distributed across various organs[57]. At the tissue microenvironment and cellular level, zinc homeostasis is tightly regulated by solute carrier transporters. The SLC39A family, also known as ZRT- and IRT-like proteins (ZIP), increases cytosolic zinc by importing it from the extracellular environment or releasing it from intracellular organelles[58]. In contrast, the SLC30A family, or zinc transporter (ZNT) proteins, reduces cytosolic zinc by transporting it into organelles or exporting it to the extracellular space[59]. Additionally, metallothioneins (MTs), small cysteine-rich proteins that bind and store zinc, provide an additional layer of regulation[60]. It is estimated that over 2,500 human proteins rely on zinc for structural integrity (e.g., zinc fingers) or biological function (e.g., cofactors)[56]. As a result, zinc plays a critical role in multiple cellular processes, including immune responses[61-68]. Thus, it is not surprising that dysregulated zinc homeostasis via altered transport and storage or systemic zinc deficiencies have been observed in multiple

malignancies[69-81]. Indeed, *in vivo* studies show that zinc supplementation can reduce tumor burden, enhance resistance to tumor challenges, and decrease the incidence of spontaneous tumors in mice[82-85], suggesting a potential therapeutic role for zinc in cancer treatment. Additionally, a recent report found that patients who respond to ICB have TAMs with metal/zinc signatures[43]. While some studies have explored the link between zinc and immunotherapy response[86-90], the results remain contradictory, and the precise molecular mechanisms underlying zinc in the TME are unclear.

Here we found that *CDKN2A*^{Low} tumor cells disrupt zinc homeostasis in the TME, driving resistance to ICB. By cross-comparing differentially regulated metabolites in the tumor interstitial fluid (TIF) and negatively enriched plasma membrane solute carrier transporter (SLCs) from a metabolism-focused *in vivo* CRISPR knockout screen, we identified zinc and the zinc importer SLC39A9 as critical for ICB resistance in *Cdkn2a*^{Low} tumors. *CDKN2A*^{Low} cells have increased plasma membrane (PM) localization of SLC39A9, leading to elevated intracellular zinc and a zinc-depleted TME. This cancer cell outcompetition for zinc leads to decreased zinc in TAMs, reducing their phagocytic activity and impairing ICB response. Restoring TME zinc levels through dietary zinc supplementation rescues TAM function and enhances ICB response. Using publicly available scRNA-Seq, we also found that zinc and phagocytosis signatures were impaired in TAMs from patients with *CDKN2A*^{Low} tumors. These findings highlight zinc homeostasis as essential for ICB efficacy in *CDKN2A*^{Low} tumors and have implications for the use of zinc supplements to improve patient outcomes.

RESULTS

Zinc and the zinc importer SLC39A9 are critical regulators of ICB resistance in *CDKN2A*^{Low} tumors

Published studies show that tumors with loss of *CDKN2A* function correlate with decreased response to anti-PD1 or anti-PD-L1 immune checkpoint blockade (ICB)[16,17,20,27,29-32]. Likewise, publicly available data show that patients with low *CDKN2A* expression (*CDKN2A*^{Low}) have shorter overall survival compared to those with high *CDKN2A* expression (*CDKN2A*^{High}) when treated with anti-PD1 or anti-PD-L1 (**Fig. S1A-B**). Notably, *CDKN2A*^{Low} patients also have shorter overall survival on anti-PD1/anti-PD-L1, even in cases where *MTAP* or *IFN* genes are expressed (**Fig. S1C-D**). To investigate the mechanism whereby loss of *CDKN2A* in cancer cells drives ICB resistance, we developed two complementary syngeneic models with *Cdkn2a* knockdown or p16 overexpression that mimic the ICB response seen in cancer patients (**Fig. 1A and Fig. S2A-J, see Methods for syngeneic mouse model details**). We and others have published that suppression of *CDKN2A*/p16 alters cell-intrinsic metabolism[4,6,7,9,10,91,92]. Excitingly, using unbiased metabolomics and metallomics in the tumor interstitial fluid (TIF), we found that multiple analytes are also differentially regulated in the TME of Yumm5.2 sh*Cdkn2a* tumors compared to controls (**Fig. 1B**). Previous studies have shown that altered cancer cell metabolism contributes to the composition and activity of immune cells within the tumor microenvironment (TME), thereby affecting tumor responses to ICB[93-96]. Thus, we reasoned that *CDKN2A*^{Low}-mediated metabolic changes in the TME may contribute to the observed ICB resistance in these tumors. To identify drivers of this phenotype, we

employed a metabolism-focused sgRNA knockout library in our Yumm5.2 isogenic cell model (**Fig. 1C**). We identified 137 genes with significant negative enrichment in sh*Cdkn2a* tumors treated with anti-PD1 vs. IgG compared to shControl tumors treated

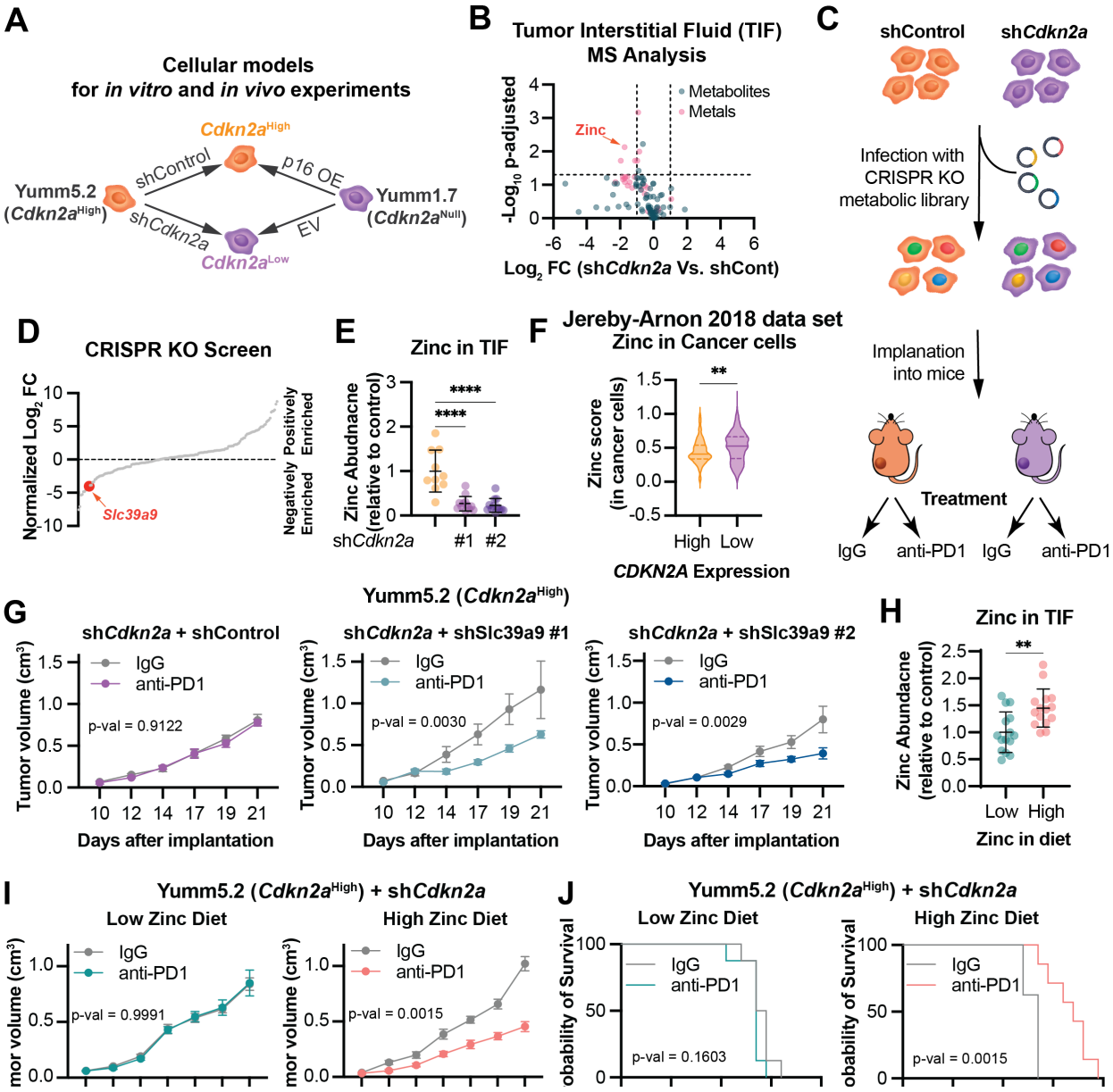

Figure 1. Zinc transport is a key determinant of ICB Response in *Cdkn2a*^{Low} tumors. (A) Schematic of cellular models. **(B)** Volcano plot of metabolites and metals in the TIF from Yumm5.2 (*Cdkn2a*^{High}) shControl and sh*Cdkn2a* tumors. **(C)** Schematic of the *in vivo* metabolic CRISPR knockout (KO) screen design. **(D)** Results from the CRISPR KO screen in mice bearing Yumm5.2 (*Cdkn2a*^{High}) shControl and sh*Cdkn2a* tumors treated with 200 µg IgG or anti-PD1 (i.p., 3x/week). Data

show Log_2 fold change (FC) of CRISPR negative score of the plasma membrane solute carrier transporters in sh*Cdkn2a* tumors treated with anti-PD1 vs. IgG vs. shControl tumors treated with anti-PD1 vs. IgG. See **Table S1**. **(E)** MS quantification of zinc levels in the TIF from Yumm5.2 (*Cdkn2a*^{High}) tumors with *Cdkn2a* knockdown (sh*Cdkn2a*, hairpins #1 and #2) or control (shCont) (n=12/group). Data represent mean ± SD. One-way ANOVA. **(F)** Zinc score in the cancer cell compartment from scRNA-Seq of melanoma patients stratified by *CDKN2A* expression. Jereby-Arnon 2018 data set. Student's t-test. **(G)** Yumm5.2 (*Cdkn2a*^{High}) cells with *Cdkn2a* knockdown (sh*Cdkn2a*) alone or combined with Slc39a9 knockdown (shSlc39a9, hairpins #1 and #2) were implanted into mice. Mice were treated with 200 µg IgG or anti-PD1 (i.p., 3x/week). Longitudinal tumor growth as mean ± SEM (n=5/group). Mixed-effects model. **(H-J)** Mice were assigned to low (55 mg/kg) or high (300 mg/kg) zinc diets. Yumm5.2 (*Cdkn2a*^{High}) cells with *Cdkn2a* knockdown (sh*Cdkn2a*) were implanted into mice. Mice were treated with 200 µg IgG or anti-PD1 (i.p., 3x/week). **(H)** MS quantification of zinc in the TIF from Yumm5.2 sh*Cdkn2a* tumors on indicated diets. Data represent mean ± SD (n=15/group). Student's t-test. **(I)** Longitudinal tumor growth as mean ± SEM (n=8/group). Mixed-effects model. **(J)** Kaplan-Meier curves (n=8/group). Log-rank (Mantel-Cox) test. * $p<0.05$, ** $p<0.01$, *** $p<0.001$, **** $p<0.0001$.

With anti-PD1 vs. IgG, indicating their requirement for inducing ICB resistance in the context of low *Cdkn2a* expression (**Table S1**). Given the role of plasma membrane solute carrier transporters in metabolite compartmentalization between the intracellular and extracellular space, we focused on these genes (**Fig. 1D and Table S2**) for cross-comparison with depleted analytes in sh*Cdkn2a* TIF (**Fig. 1B**). Using this comparison, we identified zinc and the plasma membrane zinc importer *Slc39a9* as potential drivers of ICB resistance in sh*Cdkn2a* tumors (**Fig. 1B, 1D-E**). Excitingly, *CDKN2A*^{Low} cancer cells show higher zinc scores than *CDKN2A*^{High} cells in tumors from melanoma patients (**Fig. 1F**), and ICB-treated patients with low circulating zinc levels have reduced time-to-event outcomes compared to those with higher zinc levels (**Fig. S3A**), providing additional evidence for the role of zinc in the ICB response. We validated that knockdown of Slc39a9 significantly decreased tumor volume upon anti-PD1 treatment in both *Cdkn2a*^{Low} syngeneic mouse models (**Fig. 1G and Fig. S3B-E**). Excitingly, a high zinc diet (~3X higher than normal chow) elevated TME zinc and sensitized Yumm5.2 sh*Cdkn2a* tumors to ICB

(**Fig. 1H-J**). Altogether, these data demonstrate that zinc homeostasis and Slc39a9 are essential for ICB resistance in *Cdkn2a*^{Low} tumors.

CDKN2A^{Low} cancer cells reprogram zinc homeostasis via plasma membrane SLC39A9

Next, we sought to determine how *CDKN2A* regulates zinc homeostasis via SLC39A9. Prior work found that SLC39A9 is localized in the plasma membrane and imports zinc ions from the extracellular space into the cytosol[97-101]. We found that multiple human and mouse *Cdkn2a*^{Low} cancer cell models have increased plasma membrane SLC39A9 (**Fig. 2A-B and Fig. S4A-C**). Increased plasma membrane Slc39a9 correlated with elevated intracellular zinc levels and reduced extracellular zinc levels (both labile and total), an effect that was reversed by knockdown of Slc39a9 in *Cdkn2a*^{Low} cancer cells (**Fig. 2C-E** and **Fig. S4D-G**). Overexpression of wildtype Slc39a9 rescued the intracellular labile zinc defect in Slc39a9 knockdown cells, whereas the putative loss-of-function Slc39a9^{H156R} mutant[102-104] did not (**Fig. 2F and Fig. S5A**). The lack of zinc uptake in cells expressing the Slc39a9^{H156R} mutant was not due to the inability of the mutant to localize to the plasma membrane (**Fig. 2G-H and Fig. S5B-C**). We did not observe a compensatory upregulation of other *Slc39* or *Slc30* genes (**Fig. S5D and Table S3**). Together, these data demonstrate that Slc39a9 is both necessary and sufficient for zinc uptake. Importantly, none of the metal ions commonly transported by SLC39 family members were depleted upon knockdown of Slc39a9 (**Fig. S5E**), indicating the observed changes are not due to differential uptake of other metals. Finally, we sought to determine the mechanism whereby

CDKN2A^{Low} cancer cells have increased plasma membrane SLC39A9. We did not observe differential mRNA expression of *Slc39a9* upon *Cdkn2a* knockdown or p16

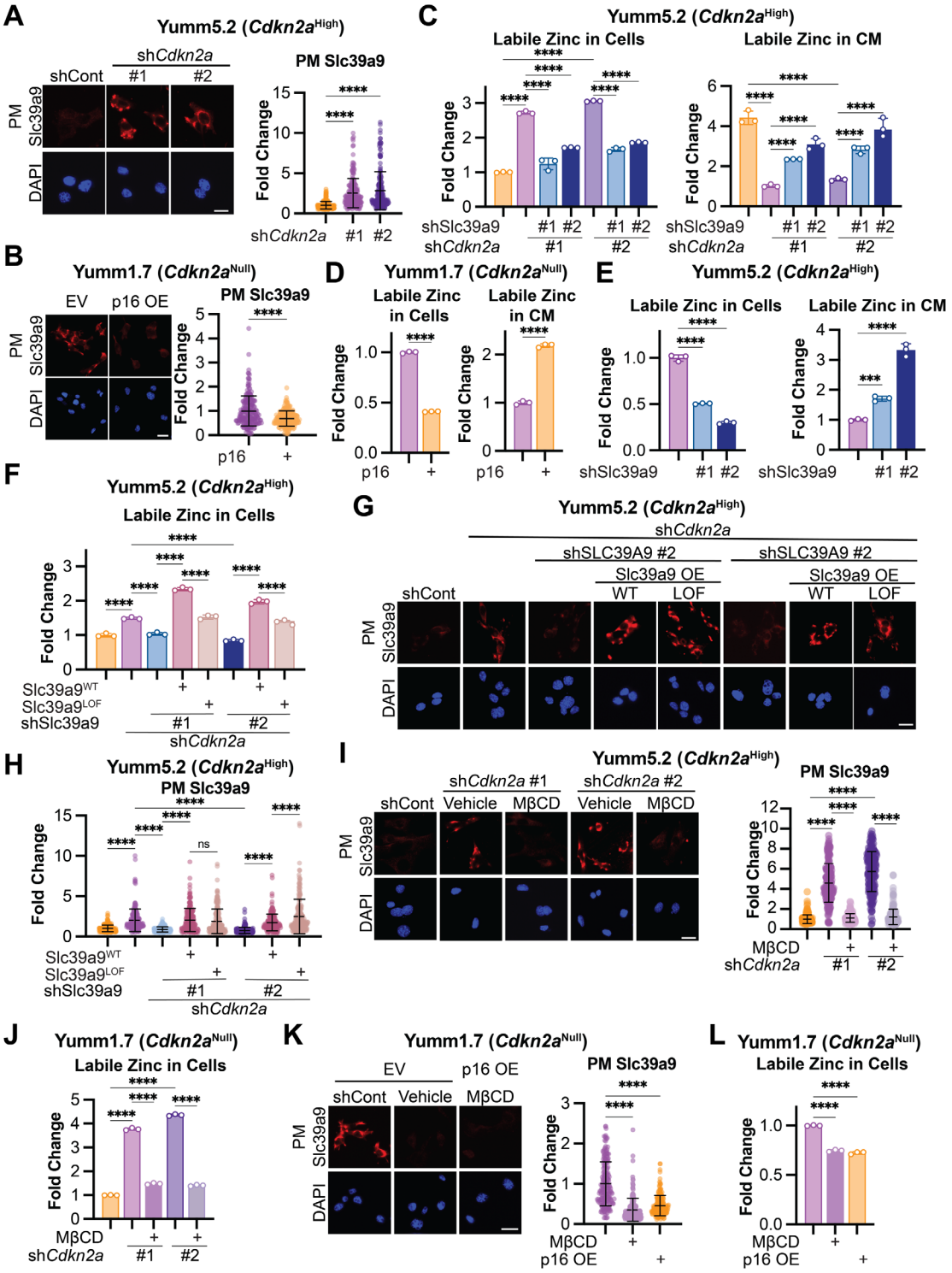

Figure 2. Increased plasma membrane Slc39a9 via cholesterol drives zinc uptake in *Cdkn2a*^{Low} cancer cells. (A-B) Representative images (left) and quantification (right) of Slc39a9 IF on non-permeabilized cells to visualize plasma membrane (PM) Slc39a9 in the indicated cells. Data represent mean ± SD (n=200/group). **(C-E)** Labile zinc quantification in cells (left) and conditioned media (CM; right) in the indicated cells. Data represent mean ± SD (n=3/group). **(F-H)** Yumm5.2 (*Cdkn2a*^{High}) cells with knockdown of *Cdkn2a* (sh*Cdkn2a*) or control (shCont) alone or in combination with knockdown of Slc39a9 (shSlc39a9, hairpins #1 and #2) and empty vector control, wildtype Slc39a9 (WT), or loss-of-function Slc39a9 mutant (LOF). **(F)** Labile zinc quantification. Data represent mean ± SD (n=3/group). **(G)** Representative images of PM Slc39a9 IF on non-permeabilized cells. **(H)** Quantification of (G). Data represent mean ± SD (n=200/group). **(I-L)** The indicated cells were treated with 10mM Methyl-β-cyclodextrin (MβCD) or vehicle for 1h. **(I)** Representative images (left) and quantification (right) of PM Slc39a9 IF on non-permeabilized cells. Data represent mean ± SD (n=200/group). **(J)** Labile zinc quantification. Data represent mean ± SD (n=3/group). **(K)** Representative images (left) and quantification (right) of PM Slc39a9 IF on non-permeabilized cells. Data represent mean ± SD (n=200/group). **(L)** Labile zinc quantification. Data represent mean ± SD (n=3/group). Scale bars = 25μm. Shown are representative data from 3 independent experiments. One-way ANOVA or student's t-test. * $p<0.05$, ** $p<0.01$, *** $p<0.001$, **** $p<0.0001$.

overexpression (**Fig. S5F**). SLC39A9 is a transmembrane protein, which are often anchored to the plasma membrane through cholesterol[105]. Our prior study found that cells with knockdown of *CDKN2A*/p16 have increased cholesterol[7]. Thus, we hypothesized that increased cholesterol levels in *CDKN2A*^{Low} cancer cells may enhance the plasma membrane SLC39A9 expression. Indeed, depletion of cholesterol using MβCD decreased plasma membrane Slc39a9 and reduced intracellular labile zinc in *Cdkn2a*^{Low} cancer cells (**Fig. 2I-L**). Altogether, these data demonstrate that *CDKN2A*^{Low} cancer cells increase intracellular zinc and deplete extracellular zinc via increased plasma membrane SLC39A9 that is regulated through cholesterol, and that SLC39A9 is a major and specific regulator of zinc homeostasis in *CDKN2A*^{Low} cancer cells.

Tumor-associated macrophages are required for ICB response in tumors with high TME zinc

We found that *Cdkn2a*^{Low} tumors, which are ICB resistant (**Fig. S2**), have depleted micro-enviromental zinc due to enhanced cancer cell zinc uptake via Slc39a9 (**Fig. 2**). Next, we aimed to determine the effects of depleted TME zinc on the immune compartment and how this affects ICB response. Given the well-established role of T cells in ICB response[106,107], we first assessed whether *Cdkn2a*^{Low} tumors with Slc39a9 knockdown remain responsive to anti-PD1 in RAG-1 deficient mice lacking T and B cells. Unexpectedly,

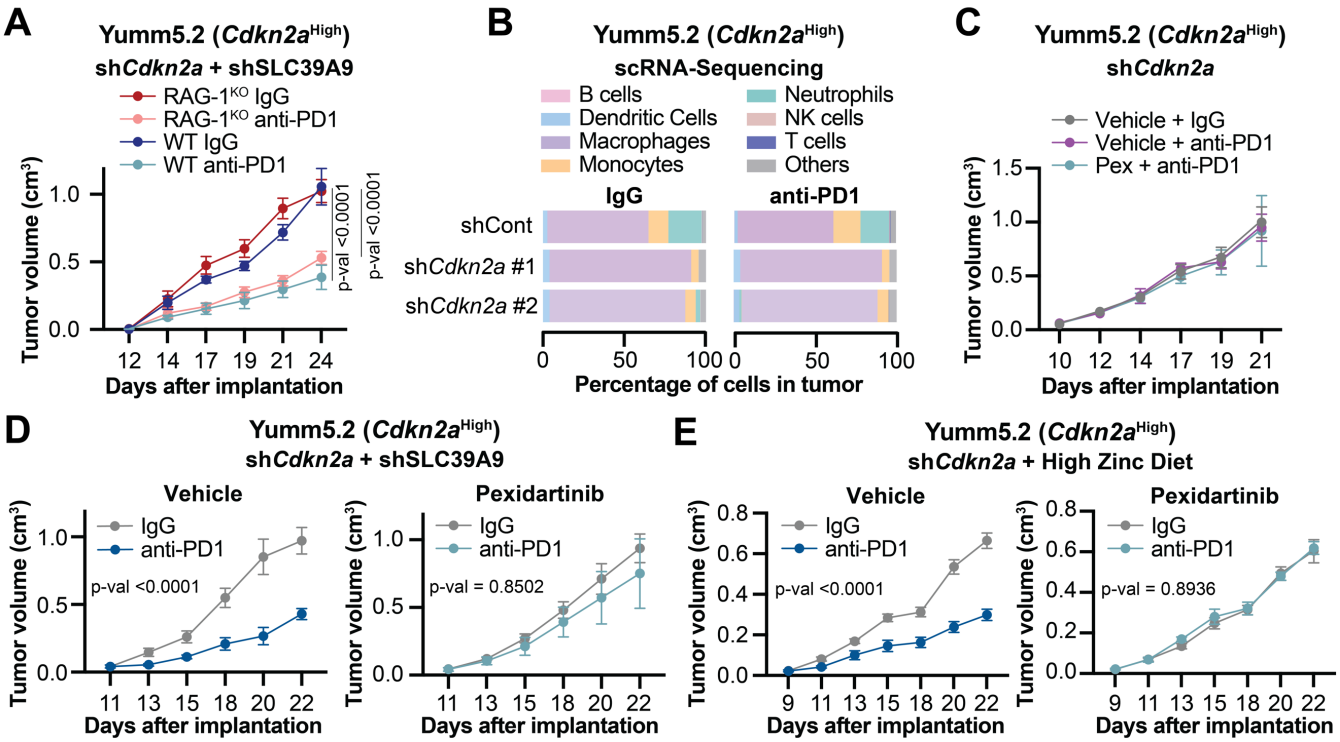

Figure 3. Macrophages drive anti-PD1 response in *Cdkn2a*^{Low} tumors upon replenishment of TME Zinc levels. (A) Yumm5.2 (*Cdkn2a*^{High}) cells with *Cdkn2a* knockdown (sh*Cdkn2a*) were implanted into wildtype (WT) and B6.129s7-*Rag1*^{tm1Mom}/J (RAG-1^{KO}) C57BL/6J mice. Mice were treated with 200 µg IgG or anti-PD1 (i.p., 3x/week). Longitudinal tumor growth as mean ± SEM (n=5/group). **(B)** scRNA-Seq of Cd45^{+} cells sorted from Yumm5.2 (*Cdkn2a*^{High}) shCont or sh*Cdkn2a* (hairpins #1 and #2) tumor-bearing mice treated with 200 µg IgG or anti-PD1 (i.p., 3x/week). Data represent the percentage of the indicated populations. **(C)** Yumm5.2 (*Cdkn2a*^{High}) cells with *Cdkn2a* knockdown (sh*Cdkn2a*) were implanted into mice. Mice were treated with 45 mg/kg of Pexidartinib (Pex) or vehicle (o.g., 3x/week) and 200 µg IgG or anti-PD1 (i.p., 3x/week). Longitudinal tumor growth as mean ± SEM (n=6/group). **(D)** Yumm5.2 (*Cdkn2a*^{High}) cells with combined *Cdkn2a* knockdown (sh*Cdkn2a*) and Slc39a9 knockdown (shSlc39a9) were implanted into mice. Mice were treated with 45 mg/kg of Pex or vehicle (o.g., 3x/week) and 200 µg IgG or anti-PD1 (i.p., 3x/week). Longitudinal tumor growth as mean ± SEM (n=6/group). **(E)** Mice were assigned to low (55 mg/kg) or high (300 mg/kg) zinc diets. Yumm5.2 (*Cdkn2a*^{High}) cells with *Cdkn2a* knockdown (sh*Cdkn2a*) were implanted into mice. Mice were treated with 45 mg/kg of Pex or vehicle (o.g., 3x/week) and 200 µg IgG or anti-PD1 (i.p., 3x/week). Longitudinal tumor growth as mean ± SEM (n=8/group). Mixed-effects model.

we found that these tumors responded to anti-PD1 in RAG-1 deficient mice to a similar extent as *Cdkn2a*^{Low} tumors with Slc39a9 knockdown in wildtype C57BL/6J mice (**Fig. 3A and Fig. S6A**), indicating that T and B cells are not essential for the ICB response in this context. To identify the immune cell populations that are altered in *Cdkn2a*^{Low} tumors, we conducted scRNA-Seq on Cd45^{+} cells in our Yumm5.2 isogenic model. Interestingly, we observed an increase in the percentage of macrophages in *Cdkn2a*^{Low} tumors, even in the absence of anti-PD1 treatment (**Fig. 3B**). This is consistent with prior observation in human tumors[17,25]. TAMs have context-dependent roles in ICB response and are often thought to be immune suppressive[108,109]. However, depletion of TAMs with the CSF1R inhibitor pexidartinib did not enhance the anti-PD1 response in *Cdkn2a*^{Low} tumors (**Fig. 3C and Fig. S6B**). Consistently, we did not observed a significant increase in the prototypical immunosuppressive genes *Mrc1* (encoding Cd206) or *Arg1*[110] in the TAMs of sh*Cdkn2a* tumors (**Fig. S6C**). However, depletion of TAMs reversed the ICB response in both sh*Cdkn2a*/shSlc39a9 tumors and in sh*Cdkn2a* tumors on a high zinc diet (**Fig. 3D-E**). These data together indicate that the TAMs in *Cdkn2a*^{Low} tumors may not be immunosuppressive and demonstrate the requirement of TAMs for ICB response in this context. Our data add to the growing body of literature on the important role of TAMs in ICB response[39,43,45,46,111-113].

The zinc-depleted TME drives dysfunctional TAMs to induce ICB resistance in *CDKN2A*^{Low} tumors

We found that TAMs are critical for the ICB response in a zinc-replete TME (**Fig. 3**). A recent publication found that increased metal signatures in TAMs, mainly genes related

to zinc function, correlate with improved ICB responses in patients[43]. Moreover, new evidence demonstrates the important role of TAMs in ICB responses at least in part via phagocytosis[39,48]. Indeed, we observed decreased zinc and phagocytosis signatures in TAMs from *CDKN2A*^{low} patient samples, including melanoma and head and neck squamous cell carcinoma (**Fig. 4A and Fig. S7A**), tumors where decreased *CDKN2A* is both

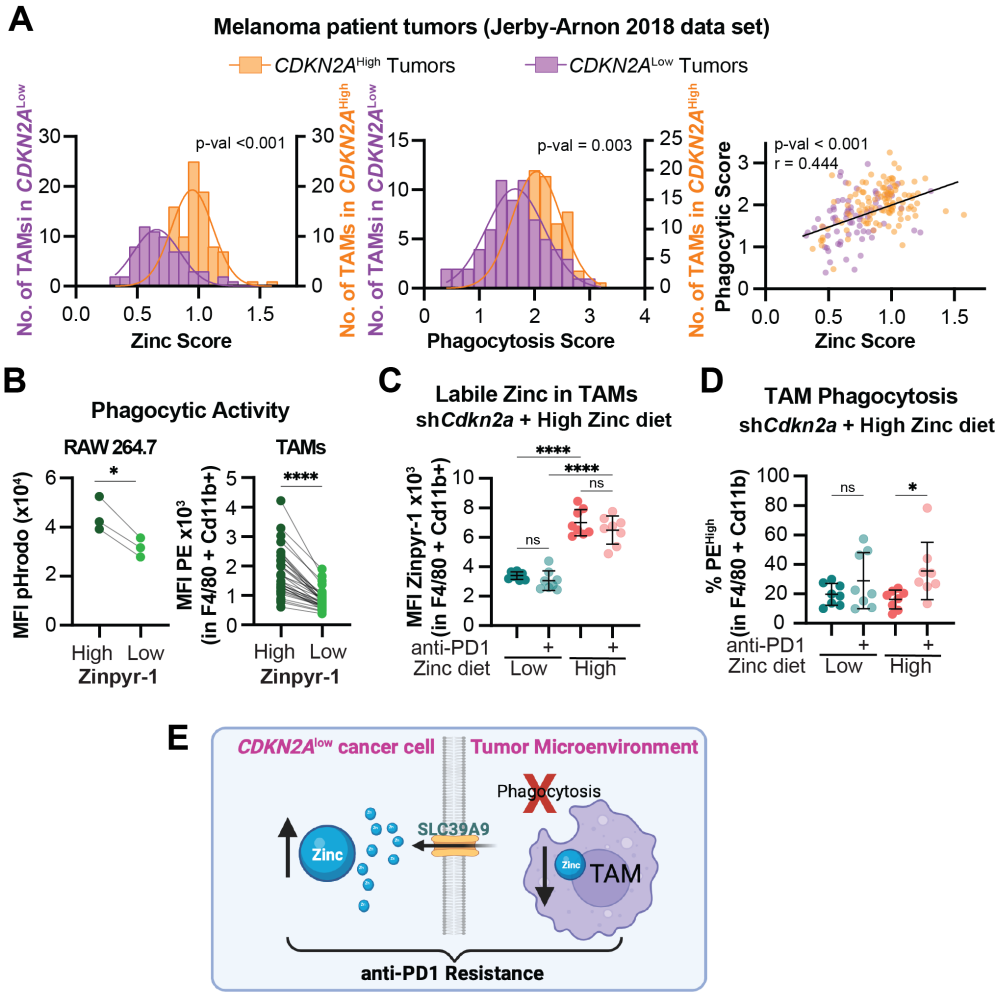

Figure 4. Replenishing TME Zinc in *Cdkn2a*^{Low} tumors re-educates TAMs and primes phagocytosis activity for ICB response. (A) Zinc and phagocytic scores calculated in the TAM compartment of melanomas harboring *CDKN2A*^{High} or *CDKN2A*^{Low} tumors in the Jerby-Arnon 2018 data set. Histogram of number of macrophages per tumor group with indicated zinc (left) or phagocytic (central) score, and their correlation (right). Linear Mixed Model. **(B)** Mean fluorescence intensity (MFI) of pHrodo in RAW 264.7 macrophages stratified based on high or low Zinpyr-1 staining of intracellular labile zinc (left). MFI of dTOMATO (PE) signal in F4/80^{+}/Cd11b^{+} TAMs stratified based on high or low

Zinpyr-1 staining of intracellular labile zinc (right). Paired student's t-test. **(C-D)** Mice were assigned to low (55 mg/kg) or high (300 mg/kg) zinc diets. Yumm5.2 (*Cdkn2a*^{High}) cells with *Cdkn2a* knockdown (sh*Cdkn2a*) or control (shCont) were implanted into mice. Mice were treated with 200 µg IgG or anti-PD1 (i.p., 3x/week). **(C)** MFI of intracellular labile zinc in F4/80+ Cd11b TAMs. One-way ANOVA. **(D)** percentage of dTOMATO (PE^{High}) cells in the F4/80+/Cd11b+ TAMs. One-way ANOVA. **(E)** Schematic of proposed mechanism. *CDKN2A*^{Low} cancer cells sequester TME zinc via increased plasma membrane SLC39A9 leading to macrophage dysfunction and ICB resistance. * $p<0.05$, ** $p<0.01$, *** $p<0.001$, **** $p<0.0001$.

common and clinically significant[1], highlighting the relevance of these pathways in humans. Consistently, further analysis of our scRNA-Seq data demonstrated that the TAMs in sh*Cdkn2a* tumors have decreased zinc signatures (**Fig. S7B**). A number of phagocytosis signatures were modestly decreased in sh*Cdkn2a* tumors compared to controls, and anti-PD1 treatment increased phagocytosis signatures in shControl tumors but failed to do so in sh*Cdkn2a* tumors (**Fig. S7C**). Thus, we reasoned that the zinc-depleted TAMs in sh*Cdkn2a* tumors are dysfunctional and hypothesize that elevating TME zinc re-educates macrophages to a pro-phagocytic phenotype to improve ICB responses in the context of low *Cdkn2a*. Indeed, we found that macrophages with more intracellular zinc are also the more phagocytic both *in vitro* and *in vitro* (**Fig. 4B**). We did not observe significative differences in "eat me" or "don't eat me" signals in sh*Cdkn2a* cells alone or in combination with shSlc39a9 (**Fig. S7D and Table S5**), suggesting this was not the cause of differential phagocytosis. Replenishing TME zinc via a high zinc diet indeed increased macrophage zinc levels (**Fig. 5C**). Excitingly, these zinc-replete macrophages had increased phagocytic activity in the context of anti-PD1 treatment (**Fig. 5D**). This was not due to changes in Pd-l1 expression on cancer cells (**Fig. S7E**)**,** indicating this is a macrophage-intrinsic effect. Altogether, these data demonstrate that *Cdkn2a*^{Low} cancer cells outcompete TAMs for zinc, leading to decreased phagocytotic function, and that increasing TME zinc re-educates macrophages to allow for a sustained ICB response (**Fig. 5E**).

DISCUSSION

The role of *CDKN2A* as a critical regulator of the cell cycle has been well established for >30 years[114,115]. However, accumulating evidence from our lab and others has revealed that *CDKN2A*/p16 has pro-tumorigenic, non-canonical functions that extend beyond its role in cell cycle control, including in metabolism[4-14,91,92]. Moreover, there is recent evidence that nutrient competition within the TME can affect immune cell activity and function[93-96]. Here, we demonstrate that loss of *CDKN2A* in cancer cells enhances zinc uptake through upregulation of the SLC39A9 transporter at the plasma membrane, a process that is mediated by cholesterol. The increased zinc uptake by *CDKN2A*^{Low} cancer cells leads to a zinc-depleted TME, impairing macrophage phagocytic activity and diminishing the efficacy of anti-PD1 treatment. Our findings underscore the critical role of *CDKN2A*/p16 expression in modulating the immune response through zinc, demonstrate an anti-tumorigenic role for zinc-replete macrophages, and open up new therapeutic possibilities through dietary interventions.

Our study demonstrates that *CDKN2A*/p16 itself drives inherent resistance to ICB. There are a handful of prior reports linking loss of *CDKN2A* expression, or 9p21 deletion, with changes in anti-tumor immunity and ICB response[5,16-32]. Here, we found that *CDKN2A*, and more specifically p16 alone, can drive differential ICB responses (**Fig. S2**). Consistent with our findings, an integrated analysis of immunogenomic and clinical data from over 1000 patients across 8 solid tumors demonstrated that 9p21 deletions, specifically encompassing *CDKN2A* and *MTAP*, were associated with decreased tumor immune

responses and resistance to anti-PD1 or anti-PD-L1 monotherapy[17]. In contrast, a prior study using cells with different 9p21 deletions showed deletions involving only the *CDKN2A* gene did not affect the response to anti-CTLA4[116]. This discrepancy may arise from differences in the models and immunotherapies used. Despite these insights, routine assessment of *CDKN2A*/p16 expression remains uncommon in clinical practice, except in specific cases such as HPV-positive tumors or when germline alterations are suspected, particularly in individuals with a family history of melanoma and/or pancreatic cancer[117-119]. Together with the prior research, our work provides compelling evidence for the need to routinely assess *CDKN2A* status in cancer diagnostics, particularly as our research suggests that treatment outcomes of patients harboring *CDKN2A*^{Low} tumors may be improved by combining ICB therapy with dietary zinc supplementation.

CDKN2A has non-canonical roles in intracellular metabolism[4,6,7,9,10,91,92], and we emphasize here a role for *CKDN2A* in influencing the metabolites within the TME. Specifically, we found that *CDKN2A*^{Low} cancer cells sequester zinc in the TME (**Fig. 2**), reducing macrophage phagocytic activity during ICB treatment, thereby diminishing ICB response (**Fig. 4**). Zinc is an essential micronutrient critical for the proper functioning of cells. For example, zinc deficiency impairs immune cell activity, while zinc supplementation can either restore normal function in deficient cells or enhance immune responses in healthy cells[120]. Despite decades of research on zinc's role in cancer, its biological effects remain poorly understood and are often contradictory[121]. These inconsistencies stem in part from a historical focus on systemic zinc levels, which overlook the intricate regulation and compartmentalized distribution of zinc within the TME. In this study, we found that increased

intracellular zinc in *CDKN2A*^{Low} cancer cells was mediated by a significant upregulation of the zinc transporter SLC39A9 at the plasma membrane (**Fig. 2**). Upregulation of plasma membrane SLC39A9 was regulated by cholesterol (**Fig. 2**), which we have previously found to be elevated in sh*CDKN2A*/shp16 cells[7]. Interestingly, several epidemiological studies have shown a strong correlation between statin use—drugs that lower cholesterol—and improved response to ICB in cancer patients[122-127]. Although outside of the scope of the present study, it is intriguing to speculate that this effect is mediated, at least in part, by decreased plasma membrane SLC39A9 in cancer cells, leading to increased zinc availability for immune cells. Moreover, these results contribute to the growing body of research highlighting the critical role of metabolite compartmentalization within the TME[93,95,128,129] and underscores the limitations of systemic zinc-level assessments in evaluating zinc's role in cancer.

Zinc can be modulated by the diet, and prior work has associated high dietary zinc intake with improved cancer outcomes or decreased risk[130-135]. However, others report adverse[136-139] or neutral effects[140-143]. Here, we found that high dietary zinc effectively increases the zinc content in the TME and improves ICB response of *Cdkn2a*^{Low} tumors (**Fig. 1H-J**). This increase in zinc in the diet is ~3X more than the normal chow. The recommended daily allowance (RDA) of zinc is 8 mg for women and 11 mg for adult men[144]. Assuming similar zinc metabolism between humans and mice, this increase in dietary zinc is equivalent to a 30 mg zinc supplement, which is available over-the-counter. Future studies are required to explore the potential benefits of combining ICB with this highly accessible and cost-effective zinc supplementation for patients with *CDKN2A*^{Low}

tumors. In contrast to our study, a recent article found that high dietary zinc promoted tumor progression in a B16F10 melanoma model by increasing regulatory T cells[88]. These differences are likely due to the amount of zinc (300mg/kg in our study vs. 80mg/kg in[88]) or delivery method. Indeed, 80 mg/kg is below our normal chow levels, suggesting that this study did not achieve high enough intratumoral zinc levels. Nonetheless, these discrepancies underscore the importance of considering tumor-specific factors, zinc delivery methods, and bioavailability when exploring zinc-based therapies. In this regard, our data show that the high zinc diet used in this study effectively increases zinc levels not only in the TME (**Fig. 1E**), but also in intratumoral macrophages (**Fig. 4C**). Although we found that replenishing the TME with zinc enhances TAM zinc content and phagocytic activity in C*DKN2A*^{Low} tumors, the role of increased intracellular zinc in *CDKN2A*^{Low} cancer cells remains unclear. The literature reports both pro-tumorigenic[145-147] and cytotoxic[148-151] effects of high intracellular zinc in cancer cells. Thus, it is interesting to speculate that zinc may have pleiotropic roles within cancer cells similar to that observed for ROS[152], where excessively high levels are detrimental, but moderate to high levels promote tumorigenesis. Further research is needed to determine the intracellular mechanisms of zinc in C*DKN2A*^{Low} cancer cells.

Our studies and others have shown that suppression of *CDKN2A*/p16 correlates with reduced expression of pro-inflammatory factors across various diseases, including cancer[5,15,153-157]. Consistently, *CDKN2A*^{Low} tumors exhibit ‘cold’ immune phenotypes with reduced immune infiltration, which has been linked to the observed resistance to ICB[17,18,22,23,25,26,158-161]. Excitingly, our findings reveal that TAMs, rather than T or B cells,

are the critical immune cell impairing the response to ICB in *CDKN2A*^{Low} (**Fig. 3**). We found that *Cdckn2a*^{Low} murine tumors have increased TAMs (**Fig. 3B**), consistent with prior reports in human patients[17,25]. However, while other research focused on the macrophage polarization status[17,21,22], here we found that *CDKN2A*^{Low} cancer cells modulate TAM phagocytic activity via rearrangement of zinc compartmentalization in the TME. In this regard, recent studies have unveiled the impact of myeloid cells—including macrophages—in orchestrating both direct and indirect responses to ICB[39,43-48]. This paradigm shift underscores the critical importance of studying TAM activity, not simply polarization status, in the context of ICB treatment to improve anti-tumor efficacy. We observed that Zinc-replate TAMs exhibited elevated intracellular zinc levels and increased phagocytic activity (**Fig. 4**). These findings align with previous research indicating that TAMs can directly respond to ICB in part via phagocytosis[39,48]. Additionally, a recent pan-cancer study in patient samples identified a subgroup of TAMs that upregulate zinc-binding metallothioneins (named *metalloMac*) that are enriched in ICB-responsive patients[43]. This is consistent with our data demonstrating that zinc metabolism in TAMs boosts the response to ICB. Indeed, zinc has been previously shown to enhance phagocytosis capacity and/or pathogen clearance[61-63,162-165], although none of this work is in cancer. Here we found that there is a correlation between the amount of intracellular zinc in TAMs and their cancer-phagocytic activity *in vivo*, both in human and mouse (**Fig. 4A-B and S7A-C**). Collectively, our findings underscore the critical role of TAM zinc metabolism in modulating the efficacy of ICB therapies, particularly in the context of *CDKN2A*^{Low} tumors, where zinc homeostasis within the TME is disrupted. This study also highlights the

potential for boosting zinc metabolism in TAMs as a strategy to enhance the therapeutic response to ICB in cancer patients.

In conclusion, the TME represents a competitive environment where access to nutrients, such as zinc, critically shapes the dynamics between tumor and immune cells. Our findings demonstrate that suppression of *CDKN2A* confers the ability to deplete zinc from the TME by upregulating the SLC39A9 transporter, impairing TAM function and reducing the efficacy of ICB therapy. This study highlights a previously unrecognized role of *CDKN2A* in maintaining a balanced TME metabolism that supports immune surveillance and therapeutic responses. In summary, our results identify an unexpected role for *CDKN2A* as a master regulator of zinc homeostasis, which impacts the TME and ICB therapy. These results have major implications not only for how *CDKN2A*^{Low} tumors are treated, but also in underscoring novel roles for *CDKN2A* outside of the cell cycle.

Supplemental Figures

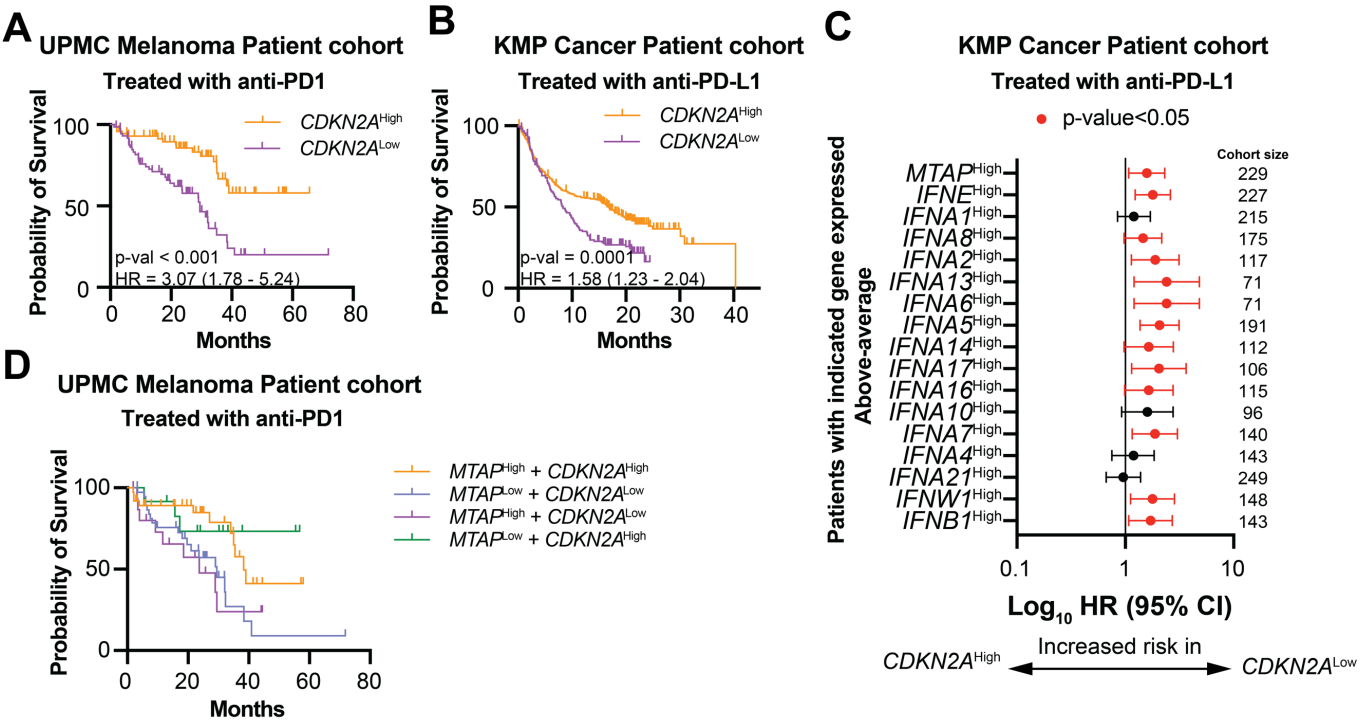

Comparison	HR (95% CI)	p-value
MTAP^{High} + *CDKN2A*^{Low} Vs. *MTAP*^{High} + *CDKN2A*^{High}	2.43 (0.89 - 6.68)	0.04
MTAP^{Low} + *CDKN2A*^{Low} Vs. *MTAP*^{Low} + *CDKN2A*^{High}	3.08 (1.28 - 7.42)	0.05
MTAP^{Low} + *CDKN2A*^{Low} Vs. *MTAP*^{High} + *CDKN2A*^{High}	2.43 (1.19 - 4.95)	0.01

Figure S1: Patients harboring *CDKN2A*^{Low} tumors have shorter overall survival on ICB. Related to Figure 1. (A) Overall survival of melanoma patients treated with anti-PD1 stratified based on *CDKN2A* expression level. UPMC Melanoma Patient Cohort. **(B)** Overall survival of cancer patients treated with anti-PD-L1 stratified based on *CDKN2A* expression level. KMP Cancer Patient Cohort. **(C)** Forest plot of hazard ratios (HR) and 95% Confidence intervals (CI) of cancer patients treated with anti-PD-L1 stratified based on *CDKN2A* expression levels but only on patients with high expression of the indicated gene. KMP Cancer Patient Cohort. **(D)** Overall survival of melanoma patients treated with anti-PD1 stratified based on *CDKN2A* and *MTAP* expression. UPMC Melanoma Patient Cohort. Log-rank (Mantel-Cox) test.

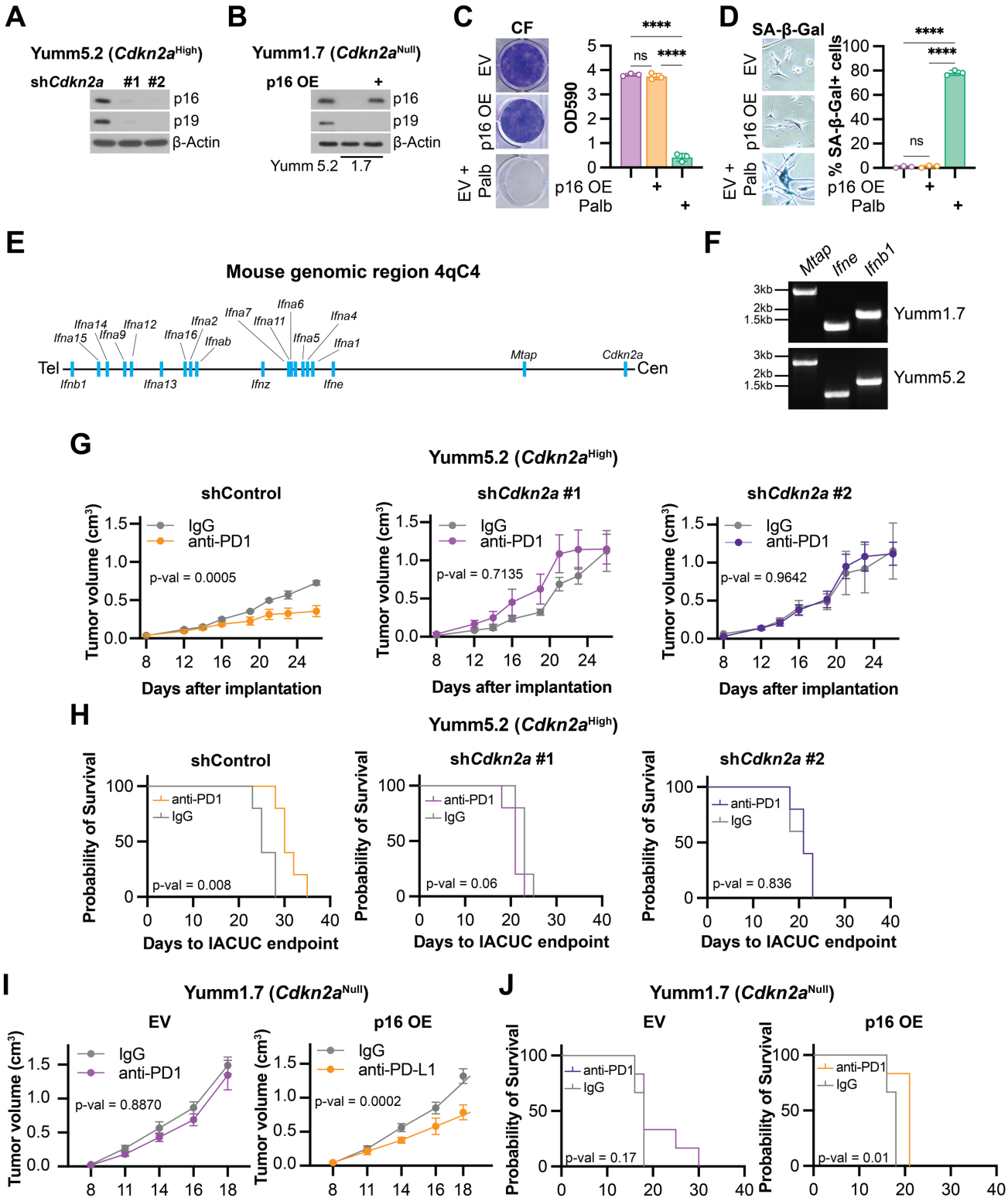

Figure S2: Cellular models used in this study. Related to Figure 1. (A-B) Immunoblot analysis of p16 and p19 in the indicated cells. β-Actin was used as loading control. **(C-D)** Yumm1.7 (*Cdkn2a*^{Null}) cells expressing empty vector (EV) control or overexpression of p16 (p16 OE). Induction of senescence with palbociclib (3 μM, 10 days) was use as positive control. **(C)** Colony

formation (CF) Assay (left) and quantification (right). One-way ANOVA. **(D)** Representative images of Senescence-Associated β-Galactosidase (SA-β-Gal) activity (left) and quantification (right). One-way ANOVA. **(E)** Schematic representation of the murine 4qC4 genomic region containing *Cdkn2a* gene and gene neighbors. **(F)** PCR amplification of indicated genes in Yumm1.7 and Yumm5.2 cell lines. **(G-H)** Yumm5.2 (*Cdkn2a*^{High}) cells expressing shControl or sh*Cdkn2a* (hairpins #1 and #2) were implanted in C57BL/6J mice and treated with 200 µg IgG or anti-PD1 (i.p., 3x/week). **(G)** Data shows longitudinal tumor growth as mean ± SEM (n=4/group). **(H)** Data shows Kaplan-Meier curves (n=5/group). **(I-J)** Yumm1.7 (*Cdkn2a*^{Null}) cells expressing empty vector (EV) control or overexpression of p16 (p16 OE) were implanted in C57BL/6J mice and treated with 200 µg IgG or anti-PD-L1 (i.p., 3x/week). **(I)** Data shows longitudinal tumor growth as mean ± SEM (n=6/group). **(J)** Data shows Kaplan-Meier curves (n=6/group). Mixed-effects model and Log-rank (Mantel-Cox) test.

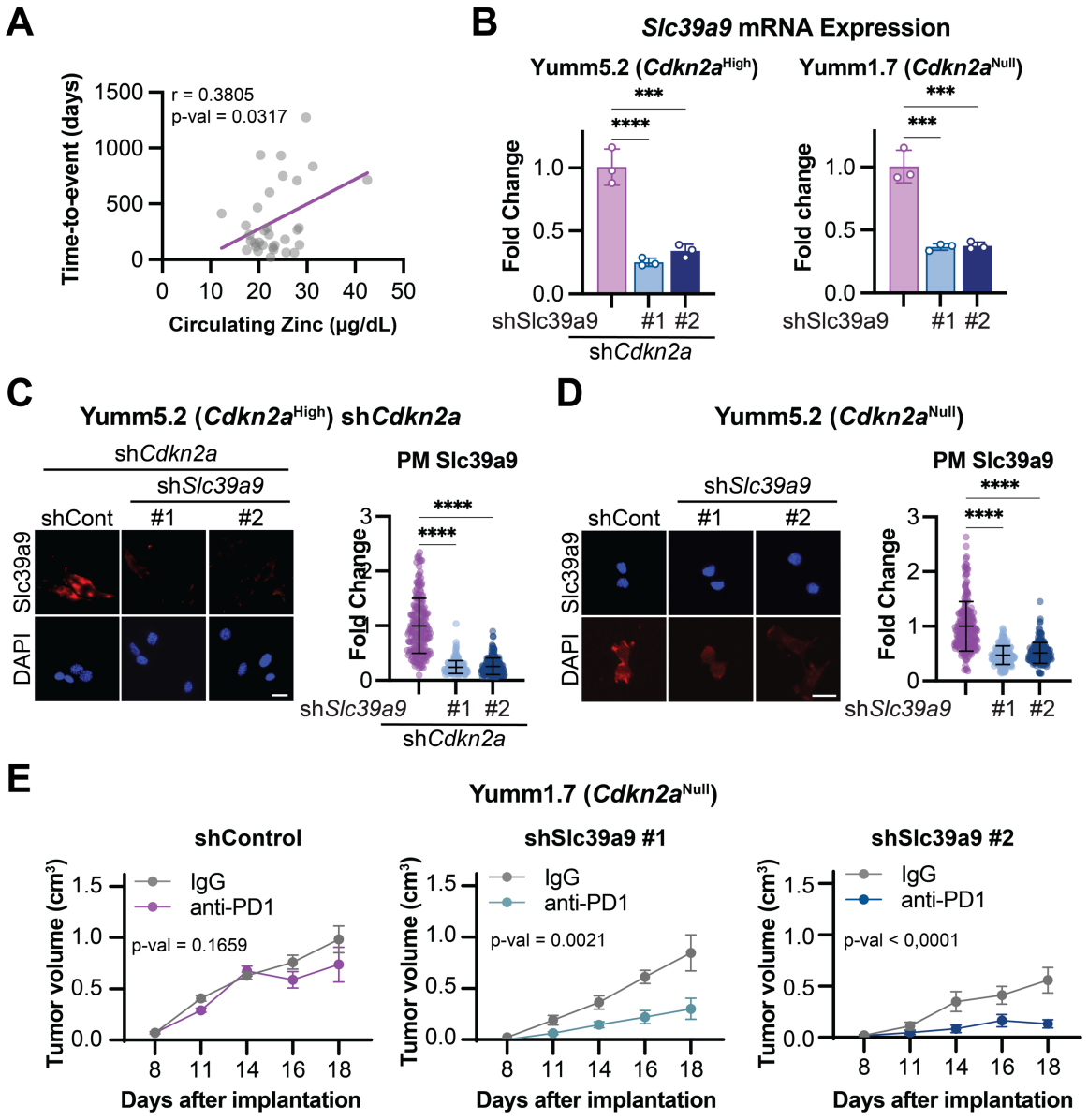

Figure S3: Circulating zinc positively correlates with time-to-event in melanoma patients treated with ICB; Replenishment of Zinc in the TME via knockdown of Slc39a9 in cancer cells restores ICB response in *Cdkn2a*^{Low} tumors. Related to Figure 1. (A) Correlation between the amount of zinc in plasma quantified by ICP-MS and the time-to-event outcome in melanoma patients from the UPMC cohort. Pearson Correlation. **(B)** *Slc39a9* mRNA expression in the indicated cell lines. Fold change to shControl group (mean ± SD). **(C)** Representative images (left) and quantification (right) of Slc39a9 IF on non-permeabilized cells. Data represent mean ± SD (n=200/group). **(D)** Same as (C), but in Yumm1.7 (*Cdkn2a*^{Null}) cells. **(E)** Yumm1.7 (*Cdkn2a*^{Null}) cells with knockdown of Slc39a9 (shSlc39a9, hairpins #1 and #2) or control (shControl) were implanted into mice. Mice were treated with 200 µg IgG or anti-PD1 (i.p., 3x/week). Longitudinal tumor growth (mean ± SEM) (n=6/group). For *in vitro* data, shown are representative data from at least 3 independent experiments. Scale bars = 25µm. One-way ANOVA and Mixed-effects model. *** p<0.005, **** p<0.001

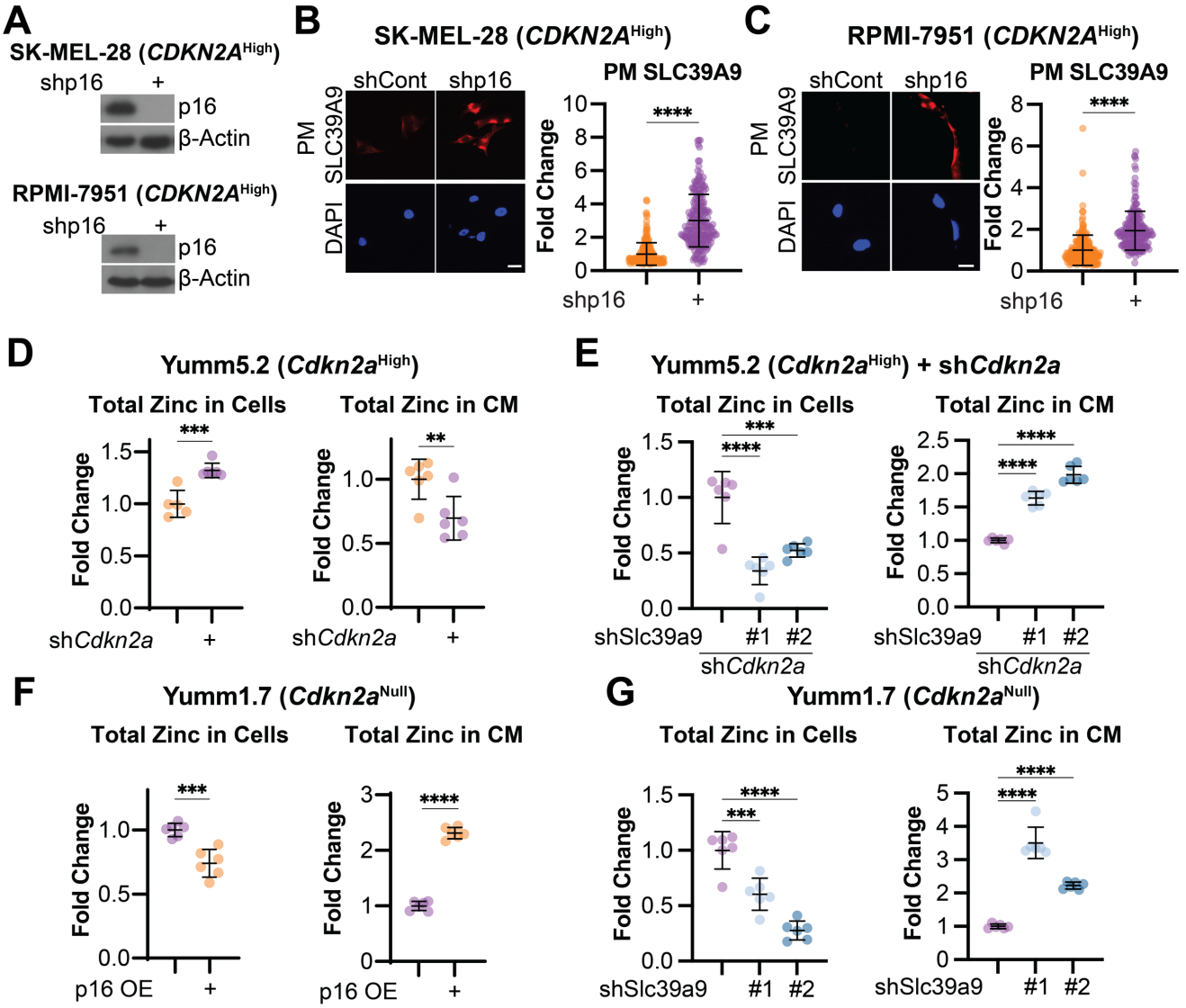

Figure S4: Knockdown of p16 in human melanoma cells increases plasma membrane SLC39A9; Slc39a9 regulates zinc uptake in *Cdkn2a*^{Low} cells. Related to Figure 2. (A) Immunoblot analysis of p16 in the indicated human melanoma cell lines. β-Actin was used as loading control. **(B)** Representative images (left) and quantification (right) of plasma membrane (PM) SLC39A9 IF on non-permeabilized SK-MEL-28 (*Cdkn2a*^{High}) cells with p16 knockdown (shp16) or control (shCont). Data represent mean ± SD (n=200/group). **(C)** Same as (A), but in RPMI-7951 (*Cdkn2a*^{High}) cells. **(D)** Total zinc quantification by ICP-MS in cells (left) and conditioned media (CM, right) in Yumm5.2 (*Cdkn2a*^{High}) cells with knockdown of Cdkn2a (sh*Cdkn2a*) or control. Data represent mean ± SD. **(E)** Same as (D) but in Yumm5.2 (*Cdkn2a*^{High}) cells with knockdown of Ckdn2a (sh*Cdkn2a*) alone or in combination with knockdown of Slc39a9 (shSlc39a9, hairpins #1 and #2). **(F)** Same as (D), but in Yumm1.7 (*Cdkn2a*^{Null}) cells overexpressing p16 (p16 OE) or empty vector control (EV). **(G)** Same as (E) but in Yumm1.7 (*Cdkn2a*^{Null}) cells. Scale bars = 25μm. Shown are representative data from 2 independent experiments. Student's t-test and one-way ANOVA. * $p<0.05$, ** $p<0.01$, *** $p<0.001$, **** $p<0.0001$.

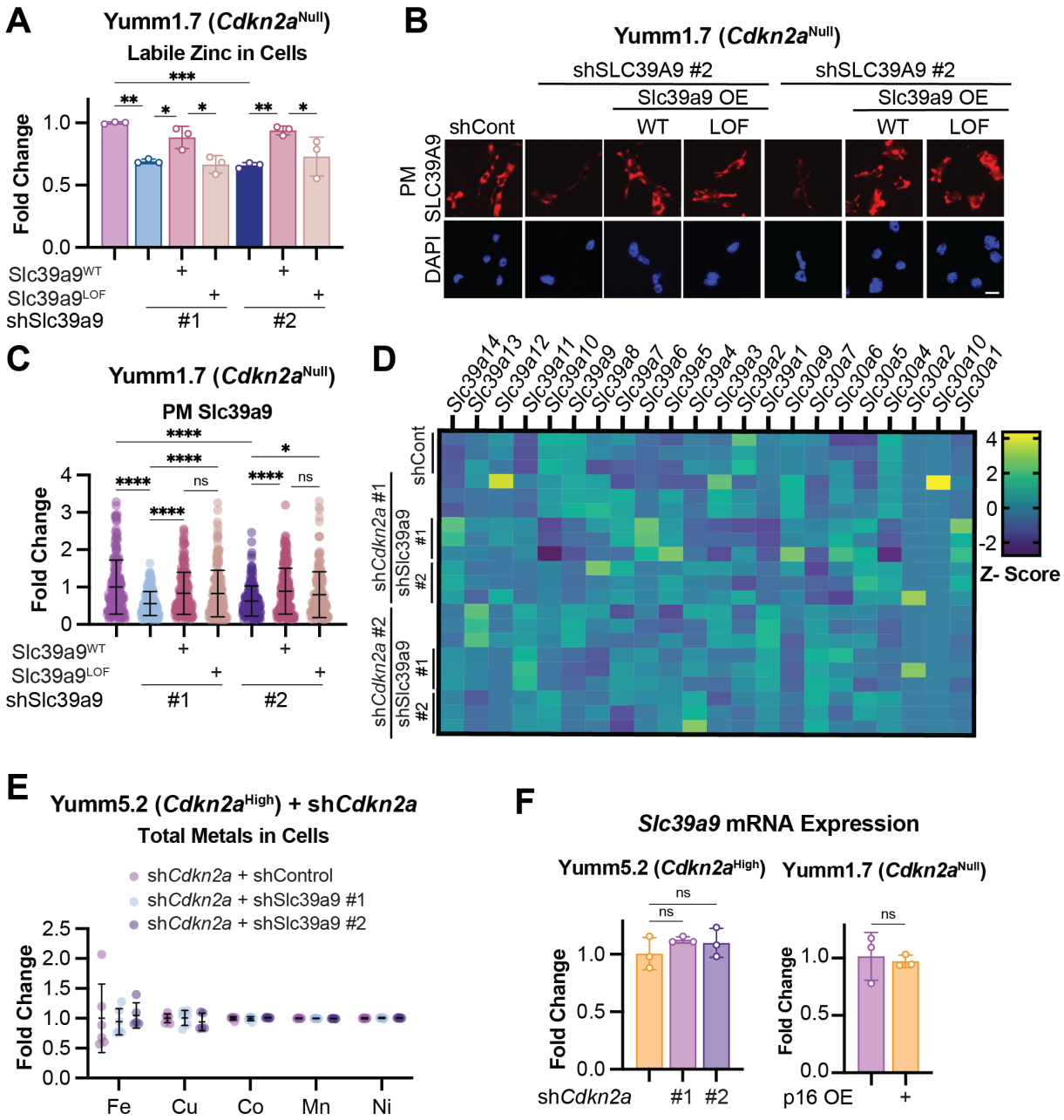

Figure S5: Slc39a9 loss-of-function mutant does not increase intracellular zinc; Knockdown of Slc39a9 does not affect other metals nor induce compensatory expression of other metal transporters. Related to Figure 2. (A-C) Yumm1.7 (*Cdkn2a*^{Null}) cells with knockdown of Slc39a9 (shSlc39a9, hairpins #1 and #2) alone or in combination with empty vector (EV) control, wildtype Slc39a9 overexpression (WT), or loss-of-function Slc39a9 mutant overexpression (LOF). **(A)** Labile zinc quantification. Data represent mean ± SD. **(B)** Representative images of plasma membrane (PM) Slc39a9 IF on non-permeabilized cells. Scale bars = 25μm. **(C)** Quantification of (G). Data represent mean ± SD (n=200/group). **(D)** Heatmap of expression values for the indicated genes in the indicated Yumm5.2 isogenic cells. **(E)** Quantification of indicated metals by ICP-MS in Yumm5.2 (*Cdkn2a*^{High}) cells with knockdown of *Cdkn2a* (sh*Cdkn2a*) alone or in combination with Slc39a9 knockdown (shSlc39a9, hairpins #1 and #2). Data represent mean ± SD. **(F)** *Slc39a9* mRNA expression in the indicated cell lines. Data represent fold change to control

group as mean ± SD. One-way ANOVA and student's t-test. * $p<0.05$, ** $p<0.01$, *** $p<0.001$, **** $p<0.0001$.

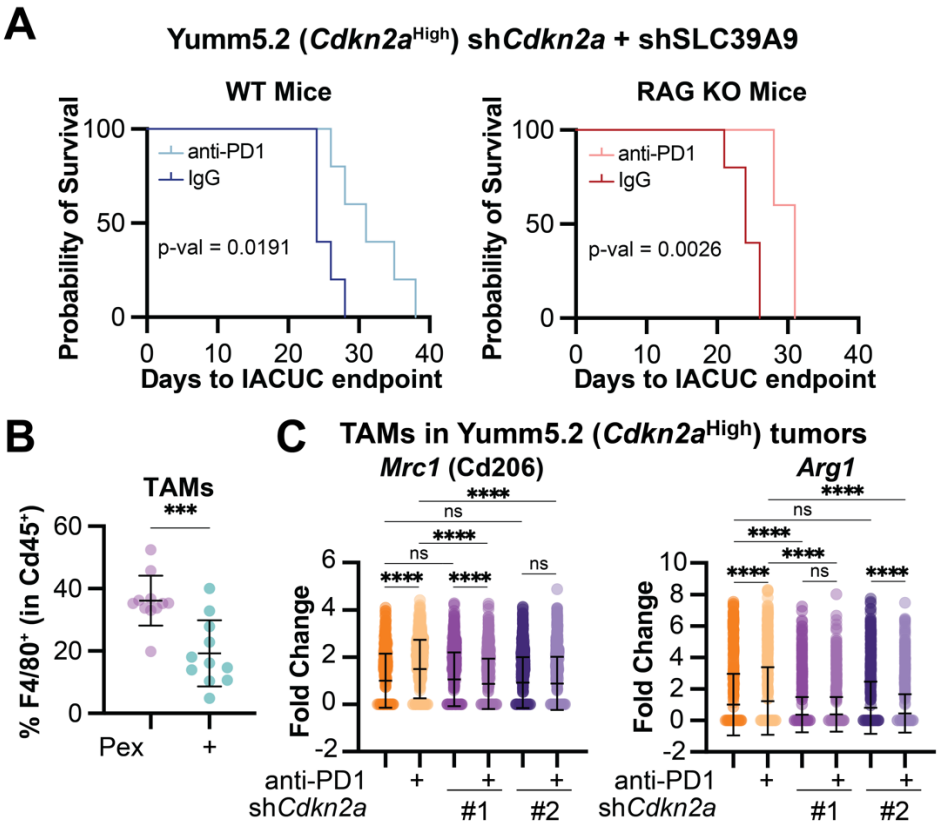

Figure S6: The restoration of ICB response upon knockdown of Slc39a9 is independent of T and B cells in *Cdkn2a*^{Low} tumors; Plexidartinib reduces tumor associated macrophages (TAMs); TAMs in *Cdkn2a*^{Low} tumors do not have increased immunosuppressive markers. Related to Fig 3. (A) Yumm5.2 (*Cdkn2a*^{High}) cells with combined knockdown of *Cdkn2a* (sh*Cdkn2a*) and Slc39a9 (shSlc39a9) were implanted into C57BL/6J wild-type (WT) and B6.129s7-*Rag1*^{tm1Mom}/J (RAG-1^{KO}) mice. Mice were treated with 200 µg IgG or anti-PD1 (i.p., 3x/week). Data represent Kaplan-Meier curves (n=5/group). Log-rank (Mantel-Cox) test. **(B)** Percent F4/80+ cells in Cd45+ cell gate in Yumm5.2 sh*Cdkn2a* tumors treated with or without Plexidartinib (Pex). Student's t-test. **(C)** mRNA expression of the prototypical immunosuppressive markers *Mrc1* (Cd206) and *Arg1* in the TAM compartment of indicated Yumm5.2 tumors. Data from scRNA-Seq represent mean ± SD of expression fold change relative to shControl. One-way ANOVA. * p<0.05, ** p<0.01, *** p<0.001, **** p<0.0001.

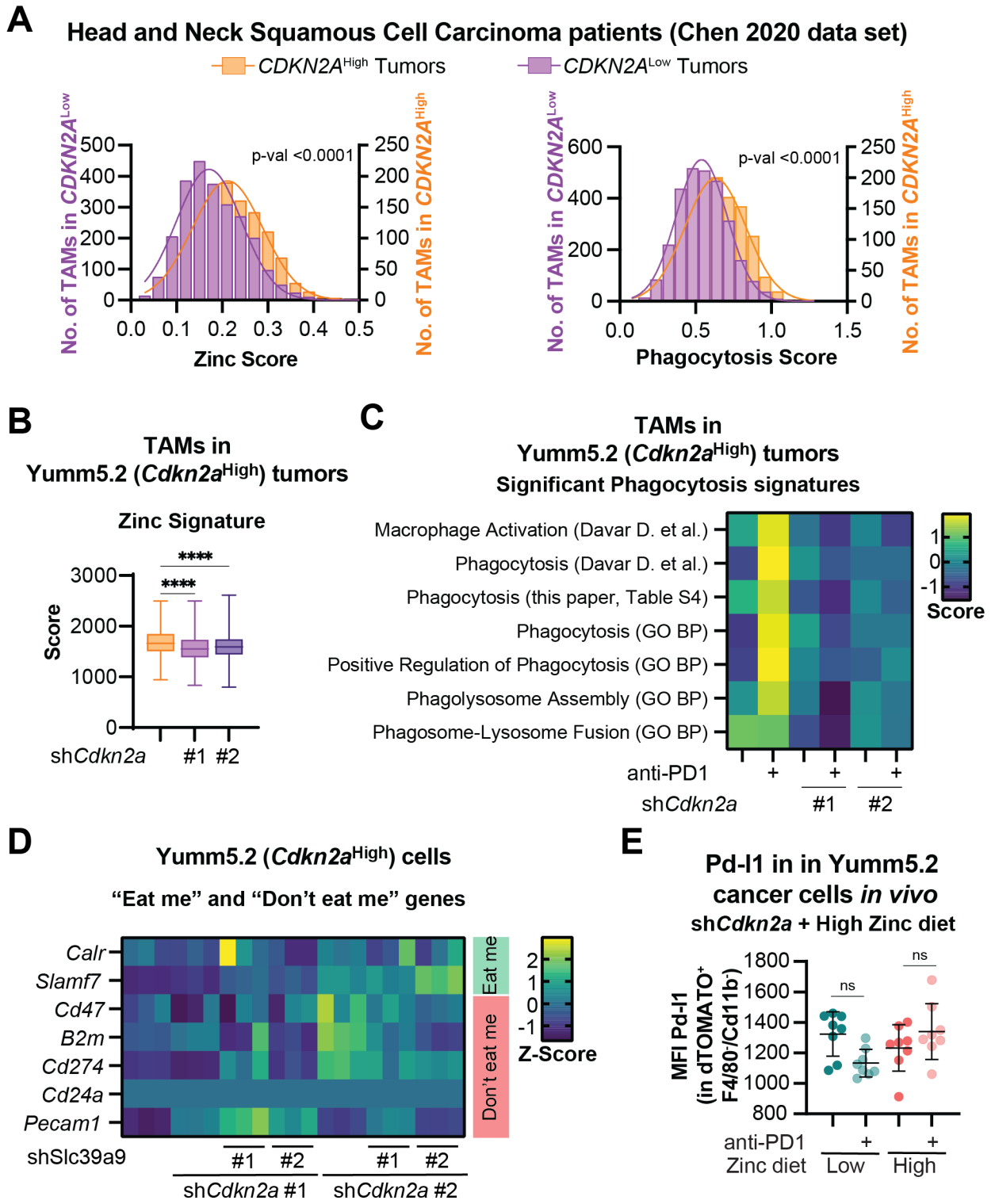

Figure S7: Tumor-associated macrophages (TAMs) in *CDKN2A*^{Low} tumors have decreased zinc and phagocytosis signatures; Knockdown of *Cdkn2a* alone or in combination with Slc39a9 knockdown does not markedly affect the mRNA expression of 'eat me' and 'don't eat me' signals; *Cdkn2a*^{Low} cancer cells do not have altered Pd-l1 expression *in vivo*. Related to Fig. 4. (A) Zinc and phagocytic scores calculated in the TAM population of indicated cancer patients harboring *CDKN2A*^{High} or *CDKN2A*^{Low} tumors. Histogram of number of

macrophages per tumor group with indicated zinc (left) or phagocytosis (right) score. Linear mixed model. **(B)** Zinc signature scores in the TAM compartment of Yumm5.2 tumors with shControl and sh*Cdkn2a* (hairpins #1 and #2). Data from scRNA-Seq represent mean ± SD. **(C)** Heatmap of scores for the indicated phagocytosis signatures in the TAM compartment of Yumm5.2 tumors with shControl and sh*Cdkn2a* (hairpins #1 and #2) treated with 200 µg IgG or anti-PD1 (i.p., 3x/week). Data from scRNA-Seq. **(D)** Heatmap of expression values for the indicated genes associated to the 'eat me' and 'don't eat me' signaling in Yumm5.2 cells with shControl and sh*Cdkn2a* (hairpins #1 and #2) alone or in combination with shSlc39a9 (hairpins #1 and #2). **(E)** Mice were assigned to low (55 mg/kg) or high (300 mg/kg) zinc diets. Yumm5.2 (*Cdkn2a*^{High}) cells with *Cdkn2a* knockdown (sh*Cdkn2a*) or control (shCont) were implanted into mice. Mice were treated with 200 µg IgG or anti-PD1 (i.p., 3x/week). Data represent mean fluorescence intensity (MFI) of Pd-l1 in cancer cells (dTOMATO+ and F4/80/Cd11b double negative. One-way ANOVA. * $p<0.05$, ** $p<0.01$, *** $p<0.001$, **** $p<0.0001$.

Acknowledgements

This work was supported by grants from the National Institutes of Health (R37CA240625 to KM. Aird, R01CA242021 to N. Hempel, R01DE031729, and P50CA254865 to R. Bao, and T32 CA082084 to BE. Dadey) and the Melanoma Research Foundation (to R. Buj). We utilized resources from the Hillman Cancer Center shared facilities, partially supported by award P30CA047904 including the Animal Facility, the Cytometry Facility (RRID:SCR_025361), the Biostatistics Facility (RRID:SCR_025355), and the Cancer Bioinformatics Services (RRID:SCR_025355). The Cancer Bioinformatics Services were additionally supported by the University of Pittsburgh Center for Research Computing, specifically the HTC high-performance computing cluster, which is supported by NIH (S10OD028483). We also used the University of Pittsburgh Single Cell Core Facility (RRID:SCR_025110), whose services and instruments were in part graciously supported by the University of Pittsburgh and the Department of Medicine. Similarly, we also used the Health Sciences Sequencing Core at UPMC Children's Hospital of Pittsburgh (RRID:SCR_023116), which resources were generously supported by the University of Pittsburgh, the Office of the Senior Vice Chancellor for Health Sciences, the Department of Pediatrics, the Institute for Precision Medicine, and the Richard K. Mellon Foundation for Pediatric Research. Finally, we extend our gratitude to Francisco J. Vazquez Moreno for his exceptional contribution to the graphic illustrations included in this paper.

Author Contributions

Raquel Buj: Conceptualization, Investigation, Methodology, Visualization, Writing – Original Draft, Review & Editing, Funding acquisition. Aidan R. Cole: Investigation,

Methodology, Writing – Review & Editing. Jeff Danielson: Investigation, Methodology. Jimmy Xu: Investigation, Methodology. Akash Kishore: Investigation, Methodology. Katarzyna M. Kedziora: Investigation, Methodology. Jie Chen: Investigation, Methodology. Baixue Yang: Investigation, Methodology, Writing – Review & Editing. David Barras: Investigation, Metodology. Apoorva Uboveja: Investigation, Methodology, Writing – Review & Editing. Amandine Amalric: Investigation, Methodology, Writing – Review & Editing. Juan J. Apiz Saab: Investigation, Methodology. Jayamanna Wickramasinghe: Investigation, Methodology. Naveen Kumar Tangudu: Investigation, Methodology, Writing – Review & Editing. Evan Levasseur: Investigation, Methodology, Writing – Review & Editing, Hui Wang: Investigation, Methodology. Aspram Minasyan: Investigation, Methodology. Rebecca E. Dadey: Investigation, Methodology. Allison C. Sharrow: Investigation, Methodology. Frank P. Venedetti: Investigation, Methodology. Dayana B. Rivadeneira: Investigation, Methodology. Christopher J. Bakkenist: Investigation, Methodology, Writing – Review & Editing. Greg M. Delgoffe: Investigation, Methodology, Writing – Review & Editing. Nadine Hempel: Investigation, Methodology, Writing – Review & Editing, Funding acquisition. Nathaniel W. Snyder: Investigation, Methodology, Writing – Review & Editing. Riyue Bao: Investigation, Methodology, Writing – Review & Editing. Adam C. Soloff: Investigation, Methodology, Writing – Review & Editing. John M. Kirkwood: Investigation, Methodology, Writing – Review & Editing. Denarda Dangaj Laniti: Investigation, Methodology, Writing – Review & Editing, Andrew V. Kossenkov: Investigation, Methodology, Writing – Review & Editing. Alexander Muir: Investigation, Methodology, Writing – Review & Editing. Jishnu Das: Investigation, Methodology, Writing – Review & Editing. Diwakar Davar: Investigation, Methodology, Writing – Review & Editing. Clementina Mesaros:

Investigation, Methodology, Writing – Review & Editing. Katherine M. Aird: Conceptualization, Investigation, Visualization, Writing – Original Draft, Review & Editing, Supervision, Project Administration, Funding Acquisition. All authors reviewed the results and approved the final version of the paper.

Declaration of Interests

The authors declare no competing interests.

MATERIAL AND METHODS

UPMC Melanoma Patient Cohort

This cohort comprises 248 cutaneous melanoma patients, pooled from five independent, publicly available studies[48,166-169], with available pre-treatment RNA-Seq and overall survival data. Details are provided in **Table S6**. Briefly, eligible patients had resectable stage III melanoma treated with neoadjuvant immunotherapy or unresectable stage III/IV treated with systemic immunotherapy. Treatment regimens included anti-PD1 monotherapy or combination therapy with anti-CTLA-4 or TLR9 agonists. Patients were stratified according to *CDKN2A* expression, either alone or in combination with *MTAP* expression (**Fig. S1A, S1D**). Expression levels of the target genes were categorized as follows: patients in or above the third tertile were considered to have high expression, while those in or below the first tertile were considered to have low expression.

Kaplan-Meier plotter (KMP) Cancer Patient Cohort:

Survival data from cancer patients was downloaded from Kaplan-Meier (KM) plotter 'Start KM Plotter for immunotherapy' (kmplot.com)[170-172] in January 2025. The analysis was performed using the following parameters: the gene symbol was set to *CDKN2A* alone (**Fig. S1B**) or in combination with Filter by median expression of patients with high expression of *MTAP* and *IFN* genes (**Fig. S1C**). Patients were split based on *lower tertile*. *Overall survival* was selected as the survival metric, with no restrictions on follow-up thresholds. The analysis was restricted to patients who had received *all anti*-PD-L1 therapy and included *all* tumor types and genders. The resulting data was exported as text for subsequent analysis in Graph Prism 10.

Cell Lines and culture conditions

All cell lines used in this study were purchased from ATCC and were used within 50 passages. ATCC performs cell line authentication by short tandem repeat (STR) profiling. Cells were cultured within 3 months of receipt or resuscitation. The murine melanoma cell lines Yumm5.2 (ATCC, catalog no. CRL-3367, RRID: CVCL_JK43) and Yumm1.7 (ATCC, catalog no. CRL-3362, RRID: CVCL_JK16) were cultured in DMEM and Ham's F-12 50/50 media (Corning, catalog no. 10-092-CV), supplemented with nonessential amino acids (Corning, catalog no. 25-025-CI). The murine macrophage cell line RAW 264.7 (ATCC, catalog no. TIB-71 ™, RRID: CVCL_0493), the human melanoma cell line SK-MEL-28 (ATCC, catalog no. HTB-72, RRID: CVCL_0526), and the human embryonic kidney cell line HEK293-FT (ATCC, catalog no. CRL-3216, RRID: CVCL_6911) were cultured in DMEM (Corning, catalog no. 10-013-CV), while the human melanoma cell line RPMI-7951 (ATCC, catalog no. HTB-66, RRID: CVCL_1666) was cultured in MEM

(Corning, catalog no. 10-009-CV). All cell lines were supplemented with 10% FBS (BioWest, catalog no. S1620) and 1% Penicillin/Streptomycin (Gibco, catalog no. 15-140-122) and maintained at 37 °C with 5% CO_2. To ensure the absence of Mycoplasma contamination, all cell lines were tested monthly as described in[173].

Plasmid information and cloning:

To perform knockdown experiments, short hairpin RNAs (shRNAs) targeting specific genes were used. The shRNA sequences employed in this study included: human shp16 (TRCN0000010482), mouse sh*Cdkn2a* #1 (TRCN0000077816) and #2 (TRCN0000362595), and mouse shSlc39a9 #1 (TRCN0000346746) and #2 (TRCN0000346750). The hairpins for shp16 and shSlc39a9 #1 and #2 were purchased pre-cloned into the lentiviral pLKO.1 vector expressing puromycin resistance (Sigma-Aldrich). The sh*Cdkn2a* #1 and #2 hairpins sequences (TRCN0000077816 and TRCN0000362595, respectively) were obtained from Integrated DNA Technologies (IDT) as desalted oligos and subsequently cloned into the lentiviral pLKO.1 vector expressing blasticidin resistance (Addgene, catalog no. 26655). Briefly, 2 µg of pLKO.1 vector were digested with 1 µL of EcoRI-HF (New England Biolabs, catalog no. R3101S), 1 µL of AgeI-HF (New England Biolabs, catalog no. R3552S), and 1 µL of rCutsmart 10X Buffer (New England Biolabs, catalog no. B6004S) in a final reaction volume of 10 µL. The digestion was incubated for 1 hour at 37°C. The linearized vector was separated by electrophoresis on a 1% agarose (IBI Scientific, catalog no. IB70070) gel and purified using the Qiagen Gel Extraction Kit (Qiagen, catalog no. 28704), following the manufacturer's instructions. Simultaneously, shRNA oligos were reconstituted to a final concentration of

100 μM in molecular-grade water (Corning, catalog no. 46-000-CM) and annealed by incubating 11.25 μL of each oligo with 2.5 μL of 10X annealing buffer (1M NaCl, 100 mM Tris, pH 7.4). The reaction was performed in a thermal cycler (Bio-Rad, T100™ Thermal Cycler, serial no. 621BR59583) starting at 95°C for 5 minutes, followed by a ramp-down to 25°C at 5°C/min. The ligation reaction was prepared by combining 50 ng of purified pLKO.1 vector with 1 μL of annealed shRNA oligos (diluted 1:400 in 0.5X annealing buffer), 1 μL of T4 ligase (New England Biolabs, catalog no. M0202T), and 1 μL of T4 ligase buffer (New England Biolabs, catalog no. B0202S) in a final volume of 10 μL. The reaction was incubated at room temperature for 3 hours, after which 5 μL of the ligation mixture was used to transform One Shot™ Stbl3™ Chemically Competent *E. coli* (Thermo Fisher Scientific, catalog no. C737303) following the manufacturer's instructions. Control lentiviral vectors, including pLKO.1-blast shGFP (Addgene, catalog no. 110419, RRID: Addgene_110419) and pLKO.1-Puro shGFP (Addgene, catalog no. 30323, RRID: Addgene_30323), were used for both human and mouse experiments. For overexpression experiments, lentiviral plasmids were synthesized by Twist Bioscience. The Twist Bioscience empty vector was used as control in overexpressing experiments. The pLX304-dTOMATO lentiviral plasmid was generously provided by the Gomes Lab at the H. Lee Moffitt Cancer Center.

Lentiviral Packaging and Infection conditions

Lentiviral vectors were packaged as follows: 10 μg of the corresponding lentiviral vector was mixed with 7.5 μg of psPAX2 (Addgene, catalog no. 12260, RRID: Addgene_12260) and 7.5 μg of pMD2.G (Addgene, catalog no. 12259, RRID: Addgene_12259) in 1.5 mL

of Opti-MEM™ media (Gibco, catalog no. 31985070) and incubated for 5 minutes at room temperature. In parallel, 50 µL of Lipofectamine™ 2000 Transfection Reagent (Invitrogen, catalog no. 11668019) was diluted in 1.5 mL of Opti-MEM™ media and incubated for 5 minutes at room temperature. The Lipofectamine mixture was added dropwise to the plasmid mixture, gently swirled to mix, and incubated for 20 minutes at room temperature. The Lipofectamine-lentiviral complexes were then added dropwise to a 60-70% confluent 10 cm dish of HEK293-FT cells, seeded 24 hours in advance and containing 7 mL of regular media, and incubated at 37°C with 5% CO2. Six to eight hours later, the media was replaced with 9 mL of fresh regular media and incubated at 37°C with 5% CO_2. Seventy-two hours later, the viral supernatants were collected, filtered through a 45 µm filter (Fisherbrand™, catalog no. 09-720-005), and used to infect target cells for 16 hours. Infected cells were selected for 3 days with 1 µg/mL puromycin (Thermo Fisher Scientific, catalog no. A1113802) for SK-MEL-28 and RPMI-7951, and 3 µg/mL puromycin and/or 3 µg/mL blasticidin (InvivoGen, catalog no. ant-bl-05) for Yumm5.2 and Yumm1.7 cells.

Mice Models

All mice were housed in a HEPA-filtered ventilated rack system at the Animal Facility of the Assembly Building of The Hillman Cancer Center, University of Pittsburgh School of Medicine. Mice were maintained on a 12-hour light/dark cycle at 21 ± 2 °C and were group-housed up to 5 mice per cage. All animal procedures were approved by the Institutional Animal Care and Use Committee (IACUC) of the University of Pittsburgh.

To investigate the role of *CDKN2A* in the response to immunotherapy, we developed two complementary subcutaneous syngeneic melanoma models. In the first model, *Cdkn2a* expression was knocked down in the *Cdkn2a*^{High} murine melanoma cell line Yumm5.2 (**Fig. S2A**). In the second model, p16 was overexpressed in the *Cdkn2a*^{Null} melanoma cell line Yumm1.7 to physiological levels that did not induce a senescence-associated phenotype (**Fig. S2B-D**). Note that Yumm1.7 cells are p19^{Null} (**Fig. S1B**)**.** Also note that both cell lines have intact *MTAP* and *IFN* gene cluster (**Fig. S2E-F**). Thus, results with this model specifically relate to p16 function. For simplicity, Yumm1.7 with p16 overexpression and Yumm5.2 cells are referred as *Cdkn2a*^{high} while Yumm5.2 with knockdown of *Cdkn2a* and Yumm1.7 cells are referred as *Cdkn2a*^{Low} cancer cells **(Fig. 1A)**. To investigate the role of SLC39A9 in resistance to anti-PD1 treatment in *Cdkn2a*^{Low} cancer cells, we used Yumm5.2 cells with dual knockdown of *Cdkn2a* and *Slc39a9* (sh*Cdkn2a*n + sh*Slc39a9*), as well as Yumm1.7 cells with *Slc39a9* knockdown (sh*Slc39a9*). In all models described above, 350,000 cells were subcutaneously implanted into the right flank of 6–8 weeks old male C57BL/6J mice (The Jackson Laboratory, strain #000664, RRID: IMSR_JAX:000664). To assess the role of T and B cells in anti-PD1 response, 350,000 Yumm5.2 sh*Cdkn2a* + sh*Slc39a9* double knockdown cells were implanted into 6–8 weeks old male B6.129s7-*Rag1*^{tm1Mom}/J mice (The Jackson Laboratory, strain #002216, RRID: IMSR_JAX:002216). In all cases, control groups received cells overexpressing corresponding shControl (shGFP) or empty vector (see *Plasmid Information and cloning* section).

In all cases described above, cells were resuspended in 200 µL DPBS (Corning, catalog no. 21-031-CV) and subcutaneously implanted using a 1 mL tuberculin syringe and a 25G needle (Becton Dickinson, catalog no. 309626). Tumor formation was monitored, and all models developed palpable tumors within 9–14 days of implantation. Tumor length (L) and width (W) were measured three times a week once palpable tumors appeared using an electronic caliper set in mm (Adoric, model number# KC24, resolution 0.1mm ± 0.2mm). Tumor volume was calculated using the formula: $\frac{1}{2}(L \times W^2)$ where $L > W$. Mouse body weight was measured weekly using an electronic scale. The experimental endpoint for longitudinal tumor growth studies was defined as the point when the first mouse reached IACUC-approved criteria: either a tumor volume exceeding 1 cm^3 or a 20% loss of body weight, whichever occurred first. For survival studies, the endpoint for each animal was similarly determined based on IACUC guidelines.

Mice treatments

For anti-PD-1 and anti-PD-L1 experiments, mice were administered 200 µg of the respective antibody or placebo, diluted in DPBS to a final volume of 200 µL, by intraperitoneal injection three times per week using insulin syringes (Excel International, catalog no. 26028). The antibodies used were: anti-mouse PD-1 (Leinco Technologies, catalog no. P362) or placebo IgG2a (Leinco Technologies, catalog no. I-1177) and anti-mouse PD-L1 (InVivoPlus™, catalog no. BP0101) or placebo IgG2b (InVivoPlus™, catalog no. BP0090). For macrophage depletion, mice were treated with 45 mg/kg Pexiclartinib (Selleck Chemicals, catalog no. S7818), diluted in a vehicle solution containing 45% PE300 (Sigma-Aldrich, catalog no. 202371), 5% Tween-80 (Sigma-Aldrich, catalog no.

P4780), and 5% DMSO (Fisher BioReagents, catalog no. BP231-100), administered via oral gavage at a final volume of 150 µL, three times per week. Treatment was delivered using a 1 mL syringe (Becton Dickinson, catalog no. 309659) and a reusable animal feeding needle (Cadence Science, catalog no. 7910; 2.5 mm ball diameter, 3.81 cm length, 20G, curved), which were autoclaved between uses. Control mice received the same volume of vehicle solution, following the same dosing schedule. All treatments described above were initiated upon detection of palpable tumors. For dietary zinc experiments, standard rodent chow (LabDiet, catalog no. 5P76) containing 110 ppm (110 mg/Kg) zinc was replaced with custom-made diets from LabDiet. Mice were fed either a high-zinc diet (LabDiet, catalog no. 5SNB) containing 300 ppm (300 mg/Kg) zinc or a low-zinc diet (LabDiet, catalog no. 5SNA) containing 55 ppm (55 mg/Kg) zinc. Both experimental diets were identical in composition to the standard chow, except for the zinc content. Mice were acclimated to the new diet for 10 to 15 days prior to tumor cell implantation and continued on the assigned diet throughout the experiment. The amount of food per cage was measured before and after replenishing the feeder two to three times per week to estimate food intake per mouse on each diet which was similar among groups.

CRISPR Drop out Screen

The pooled mouse metabolic-focused CRISPR KO library was a gift from Dr. Kivanc Birsoy (Addgene, catalog no. 160129). Fifteen million Yumm5.2 cells expressing sh*Cdkn2a* or control shGFP were infected with pooled CRISPR KO library to an MOI <0.25 to achieve ~500-fold library coverage after selection with 3 µg/mL puromycin. The cells were passaged every 2–3 days for two weeks, maintaining the full population, before

implantation into mice. A total of 350,000 cells per mouse were injected into 36 mice per group, achieving a 550-fold library coverage. Mice were treated with either anti-PD1 or IgG as described in the *Mice Treatments* section above. Once tumors reached 0.5 cm^3, they were harvested, and DNA was isolated using the Quick-DNA Miniprep Plus kit (Zymo Research, catalog no. D4069) following the manufacturer's instructions. DNA from each mouse in the same group was pooled and used for gRNA amplification. To ensure adequate gRNA representation, calculations from Wohlhieter et al.[174] were used to achieve >450-fold coverage. In brief, 64 µg of genomic DNA per condition was divided into 16 PCR reactions, with 4 µg per reaction. The gRNA region was amplified using primers listed in **Table S7** and Ex Taq DNA polymerase (Takara, catalog no. RR001A) following the manufacturer's protocol. The PCR conditions were as follows: one cycle at 94 °C for 2 minutes, followed by 30 cycles of 94 °C for 20 seconds, 63 °C for 30 seconds, and 72 °C for 45 seconds, concluding with a final extension step at 72 °C for 1 minute. The reaction was performed in a thermal cycler (Bio-Rad, T100™ Thermal Cycler, serial no. 621BR59583). The resulting PCR amplicons were purified using the Wizard® SV Gel and PCR Clean-Up System (Promega, catalog no. A9282) following the manufacturer's instructions and pooled. The cleaned amplicons were sequenced using a NextSeq high output 75 cycle kit 1x50 in an Illumina NextSeq 500 (Serial no. NB: 501446). Data was analyzed using the MAGeCK bioinformatics pipeline to identify negatively enriched genes (Li et al., 2014). **Fig. 1D** shows the Log_2 fold change of the negative CRISPR score of solute carrier transporter in YUMM5.2 sh*Cdkn2a* tumors in mice treated with anti-PD-1 vs. IgG vs. shControl tumors in mice treated with anti-PD-1 vs. IgG.

Isolation of plasma and tumor interstitial fluid (TIF)

Mouse blood was collected via lancet check bleed (Braintree Scientific, catalog no. GR 4MM) into EDTA tubes (SAI Infusion Technologies, catalog no. K3EDTA). Plasma was separated by centrifugation at 1500g for 10 minutes at 4°C and stored at -80°C for later analysis. After bleeding, animals were euthanized by cervical dislocation, and tumors were harvested, weighed, rinsed briefly in saline (150 mM NaCl), and excess saline removed using filter paper (Cytiva, catalog no. 1001-813). TIF was isolated using a previously described centrifugal method[175]. Briefly, tumors were placed on a 20 µm strainer (pluriSelect, catalog no. 43-50020-03) within a sterile 50 mL conical tube (FisherbrandTM, catalog no. 06-443-19) and centrifuged at 11,000g for 10 minutes at 4°C. TIF was collected from the conical tube, rapidly frozen in liquid nitrogen, and stored at -80°C. TIF volumes ranged from 5 to 100 µL, <20% of the tumors did not yield any fluid. The interval from euthanasia to centrifugation was <2 minutes per mouse.

Quantification of metabolite levels

LC/MS was performed using a QExactive orbitrap mass spectrometer using an Ion Max source and heated electrospray ionization (HESI) probe coupled with a Dionex Ultimate 3000 UPLC system (Thermo Fisher). External mass calibration was set every 7 days and internal mass calibration (lock masses) was not used. The mass spectrometer was operated in full-scan, polarity switching mode with the spray voltage set to 3.0 kV, the heated capillary held at 275 °C, and the HESI probe held at 350 °C. Seath gas flow rate was set to 40 units, the auxiliary gas flow at 15 units, and the sweep gas flow at 1 unit. Data

acquisition was performed in a range of 70 to1000 *m/z*, with resolution set to 70,000, the AGC target at 1e6, and the maximum injection time at 20 milliseconds.

A library of 149 chemical standards of plasma polar metabolites was built as we have previously described (see first paragraph of *Quantification of metabolite levels in TIF and plasma* from the methods section in Sullivan MR et al. article[175]). Polar metabolites were extracted from 5 µL of each sample using 45 µL of a solvent mixture consisting of acetonitrile, methanol, and formic acid (75:25:0.1), which included isotopically labeled internal standards (ISTDs). Samples were vortexed at 4°C for 10 minutes and centrifuged at 15,000g for 10 minutes to separate the supernatant containing soluble polar metabolites. Aliquots of 2 µL of sample were injected onto a ZIC-pHILIC (2.1x150 mm) analytical column equipped with a guard column (2.1 x 20mm), both of 5 µm particle size (EMD Milipore). Column was maintained at 25°C and the autosampler was set at 4°C. The mobile phase consisted of Buffer A (20 mM ammonium carbonate, pH adjusted with ammonium hydroxide), and Buffer B (acetonitrile). The chromatographic gradient was run at a flow rate of 0.150 mL/minute as follows: 0–20 min: linear gradient from 80% to 20% B; 20–20.5 min: linear gradient from 20% to 80% B; 20.5–28 min: hold at 80%. All solvents used in this protocol were LC/MS gradient.

Metabolite identification was performed using XCalibur 2.2 software (Thermo Fisher Scientific), applying a 5 ppm mass accuracy window and a 0.5-minute retention time window. External standard pools were used for metabolite peak identification based on *m/z* values and retention times. The limit of detection ranged from 100 nM to 3 µM, depending on the

metabolite. For metabolite quantification, two methods were used: stable isotope dilution for metabolites with available ISTDs, and external standard calibration for those without Briefly, for stable isotope dilution quantification, peak areas of labeled ISTDs were compared to external standard pools to determine their concentration. The peak area of each unlabeled metabolite in the TIF and plasma samples was then compared to the quantified ISTDs to calculate metabolite concentrations. For metabolites without ISTDs, quantification by external calibration involved normalizing the peak area of each analyte to that of a labeled ISTD to account for sample recovery differences. This normalization was applied to both biological samples and external standard pool dilutions. A standard curve was generated from the normalized peak areas, with linear fits typically above $r^2 = 0.95$. These curves were used to convert peak areas in TIF or plasma samples into metabolite concentrations. These the results are considered semiquantitative due to matrix differences between external standards (prepared in water) and the samples. Please, refer to *Quantification of metabolite levels in TIF and plasma* from the methods section in Sullivan MR et al. article[175] for more details.

Harvest cells and conditioned media for ICP-MS and labile zinc quantification

For ICP-MS and labile zinc quantification, cells were seeded in 10 cm tissue culture dishes (Cellstar, catalog no. 82050-916) at densities of 500,000 and 300,000 cells per dish, respectively. Cells were seeded in complete media and incubated for 48 hours (refer to the *Cell Lines and Culture Conditions* section for details). After this initial incubation, cells were washed twice with DPBS, and the media was replaced with 6 mL of FBS-free DMEM and Ham's F-12 50/50 media (Corning, catalog no. 10-092-CV) and incubated for

an additional 24 hours. Conditioned media was filtered through a 0.45 μm filter (Fisher-brand™, catalog no. 09-720-005), aliquoted, snap-frozen in liquid nitrogen, and stored at -80°C until analysis.

For ICP-MS, attached cells were washed twice with ice-cold DPBS, scraped into 1 mL of 80% methanol (Fisher Scientific, catalog no. A456-4) over dry ice, snap-frozen in liquid nitrogen, and stored at -80°C until analysis. For Labile Zinc Quantification, attached cells were washed twice with room-temperature DPBS, scraped into 1 mL of room-temperature DPBS, and immediately processed for staining. Six and three replicates per condition (for both cells and conditioned media) were harvested for ICP-MS and labile zinc quantification, respectively. In both cases, two additional plates were cultured in parallel to estimate the cell number at the end of the experiment, which was used to normalize zinc levels per cell. Cell counts were determined using a hemocytometer, by counting four squares in two independent aliquots taken from the same sample and averaging the results.

Quantification of metals levels

Human and Mouse Plasma and Mouse TIF were collected as described in the *Isolation of Plasma and Tumor Interstitial Fluid (TIF)* section. *In vitro* cells and conditioned media were collected as outlined in the *Harvesting Cells and Conditioned Media for ICP-MS and Labile Zinc Quantification* section. For cells collected in 80% methanol, the methanol was evaporated to dryness under nitrogen gas prior to further processing. All samples including methanol-evaporated cells, conditioned media, TIF, and plasma, were spiked with 159Tb and 89Y (High-Purity Standards, catalog nos. 1057-1 and 1067-1, respectively) as

ISTDs to final concentrations of 0.2 ppb and 1 ppb, respectively. ISTDs were used to correct variations in sample preparation and to monitor fluctuations during the ICP-MS acquisition. Samples were digested with 250 µL of concentrated nitric acid (Fisher Chemical™, catalog no. A509P500) at 50°C for 16 hours. Following digestion, samples were diluted to a final volume of 5 mL with metal-free water (produced using a Milli-Q system, Millipore Sigma, catalog no. IQ7003). Multi-element metal standard calibration curves were generated at the same time with each batch of samples, using a premixed metal ion stock solution (High-Purity Standards, catalog no. QCS-27-100), using the exact sample procedure as for the samples. The calibration curves used ½ serial dilutions ranging from 250 ppb to 0.12 ppb, and were spiked with same amount of ISTD as the samples. Quality controls were prepared by exactly same protocol as the samples, and were ran at the beginning and the end of the analysis of each batch, to verify measurement accuracy thorough the batch. The limit of quantification for each metal was determined for each batch, and was usually 0.12 ppb or 0.24 ppb, depending on the batch. All solvents used in the protocol were of LC/MS or TraceMetal grade. All samples, including controls, were prepared in 15 mL polypropylene tubes (Fisher Scientific; catalog no. 14-955-238).

Metal quantification was performed using an iCAP RQ ICP-MS (Thermo Scientific, serial no. ICAPRQ01408) equipped with a Cetac ASX-560 autosampler (Teledyne Cetac Technologies). The ICP-MS system was operated under constant argon plasma gas flow at 110 psi. Elemental detection was performed in kinetic energy discrimination (KED) mode using helium gas at 17 psi. Data for each sample were acquired in triplicate, and averaged values were reported.

Labile Zinc quantification

Cells and conditioned media were collected as outlined in the *Harvesting Cells and Conditioned Media for ICP-MS and Labile Zinc Quantification* section. One million scraped cells were pelleted in a round-bottom 96-well plate (Corning, catalog no. 3366) by centrifugation at 350 g for 5 minutes at 4°C. Cells were then stained with 50 μM Zinpyr-1 (Cayman Chemical, catalog no. 15122) diluted in DPBS, containing a 1:1000 dilution of Live/Dead Fixable Near-IR Dead Cell Stain kit (Invitrogen, catalog no. L34976), in a final volume of 50 μL for 20 minutes at 4°C, protected from light. Following staining, cells were fixed in 4% paraformaldehyde (Sigma Aldrich, catalog no. 158127-3Kg) for 15 minutes at 4°C, shielded from light, and resuspended in FACS buffer (1x PBS, 10 mM HEPES [Gibco, catalog no. 15630080], 1% heat-inactivated FBS [Sigma Aldrich, catalog no. F4135-100ML], 0.05% sodium azide [Sigma Aldrich, catalog no. S2002-25G]). Stained cells were immediately analyzed on a CytoFlex Flow Cytometer (Beckman Coulter, serial no. 822338373). Flow cytometry data were analyzed with FlowJo version 10. The median fluorescence intensity (MFI) of single live cells was measured to assess intracellular zinc levels per sample.

Labile zinc concentration was measured as previously described[176]. Briefly, 50 μL of conditioned media was mixed with 50 μL of 50 μM Zinpyr-1 (Cayman Chemical, catalog no. 15122) in a 96-well polystyrene microplate (Greiner Bio-One, catalog no. 655101). The mixture was incubated for 20 minutes at 37°C in a CO_2 incubator. Fluorescence was then measured in a fluorescent plate reader (Promega GloMax explorer, serial no.

9720100141) with excitation at 475 nm and emission at 500-550 nm. This first fluorescence measurement reflects the signal of Zinpyr-1 bound to zinc in the sample (F). To determine the baseline fluorescence, 50 µL of 600 µM of the zinc chelator N,N,N',N'-tetrakis(2-pyridinylmethyl)-1,2-ethanediamine (TPEN, MilliporeSigma, catalog no. 6163941100MG), was added to each well. After another 20-minute incubation at 37°C in a CO_2 incubator, fluorescence was measured again, representing the minimum fluorescence (F_{min}) due to the chelation of zinc. Finally, to obtain the maximum fluorescence (F_{max}), 50 µL of 2 mM $ZnSO_4$ (Sigma Aldrich, catalog no. Z2876-500ML) was added to each well. After a final 20-minute incubation at 37°C in a CO_2 incubator, the fluorescence was measured one last time. The zinc concentration in each sample was then calculated using the formula: Zn^{2+} concentration = $K_D \times ((F - Fmin) / (Fmax - F))$, where K_D is the dissociation constant of the zinc:Zinpyr-1 complex (0.7 nM)[176]. Finally, zinc concentrations were normalized to the number of cells in each sample at the time of harvesting.

Immunofluorescence (IF)

Approximately 30,000 to 50,000 cells were seeded onto coverslips in 12-well plates (Corning, catalog no. 3513) and incubated at 37°C with 5% CO_2. Specifically, Yumm1.7 cells, which have low attachment properties, were seeded onto poly-L-ornithine-coated coverslips to enhance cell adhesion. Briefly, coverslips were first washed with 2 mL of 200 proof ethanol (Decon Labs) for 5 minutes, followed by two washes with molecular-grade water (Corning, catalog no. 46000CM). Then, 500 µL of poly-L-ornithine (Sigma Aldrich, catalog no. P4957-50mL) was added to each well containing a coverslip. The plates were sealed with parafilm (VWR, catalog no. 52858-032) to prevent evaporation,

and incubated overnight at 37°C. Before seeding the cells, the coverslips were washed three times with 1 mL of molecular-grade water and air-dried for 10 minutes. Approximately 16 hours after seeding, the cells were fixed with 4% paraformaldehyde (Sigma Aldrich, catalog no. 158127-3Kg) for 10 minutes. If necessary, cells were permeabilized with 0.2% Triton X-100 (VWR, catalog no. 97062-208) for 5 minutes. For plasma membrane staining of SLC39A9, however, permeabilization was omitted. The cells were then blocked with 5 µg/mL of CD16/CD32 (Invitrogen, catalog no. 14016185) diluted in 3% BSA/PBS (Fisher BioReagents, catalog no. BP1600) for 10 minutes. Both human and mouse cells were subsequently incubated with 10 µg/mL of anti-Slc39a9 (Thermo Scientific, catalog no. PA521074), diluted in 3% BSA/PBS for 1 hour. After incubation, the cells were washed three times with PBS and then incubated with 0.75 µg/mL of secondary anti-rabbit Cy3-conjugated antibody (Jackson ImmunoResearch, catalog no. 111-165-003), diluted in 3% BSA/PBS for 1 hour in the dark. For permeabilized staining, cells were washed three times with 1% Triton X-100, while non-permeabilized cells were washed 10 times with PBS to ensure complete removal of antibodies before permeabilization. Cells were then permeabilized with 0.2% Triton X-100 for 5 minutes. Cells were stained with 0.15 µg/mL DAPI (diluted in PBS) for 1 minute. Finally, coverslips were mounted (Sigma Aldrich, catalog no. F6182-20ML) and sealed with transparent nail polish. Controls included staining with 10 µg/mL normal rabbit IgG (Cell Signaling, catalog no. 2729) and secondary-only staining.

Five to ten images were captured per condition using an inverted microscope (Nikon ECLIPSE Ti2, serial no. 542740) equipped with a 20x/0.17 objective (Nikon DIC N2 Plan

Apo), a digital camera (ORCA-Fusion, catalog no. C1440-20UP, serial no. 000670) and the NIS-Elements AR software. The images were processed using ImageJ, and SLC39A9 quantification was conducted as follows: Images of nuclear staining (DAPI) were normalized between the 3rd and 97th percentiles before segmentation, which was performed using a pre-trained CellPose model "cyto"[177]. Nuclei touching the image borders were excluded from the analysis. The total number of segmented nuclei per condition was determined, and the Cy3 fluorescence signal (anti-Slc39a9) was measured in the nuclear regions. Background correction was applied by subtracting the median signal of the entire image. The median fluorescence intensity for each cell in each image was calculated. Finally, the number of cells per condition was randomized, and 200 cells per condition were plotted as fold change relative to the control.

Methyl-β-cyclodextrin (MβCD) treatment

Cells seeded in 12-well plates (Corning, catalog no. 3513) for immunofluorescence (IF) or in 6 cm plates (Falcon, catalog no. 353002) for flow cytometry were treated with 10 mM MβCD (Sigma Aldrich, catalog no. C4555-10G) diluted in FBS-free DMEM and Ham's F-12 50/50 media (Corning, catalog no. 10-092-CV), supplemented with 10 mM HEPES (Gibco, catalog no. 15630080). The treatment was carried out for 1 hour at 37°C with 5% CO_2. After treatment, cells were collected for downstream analysis, such as IF or labile zinc quantification. Note that MβCD-treated cells are extremely loosely adhered, so washes must be done gently. To prevent cell loss during the immunofluorescence staining procedure, fixation time was increased to 20 minutes.

Tumor cell disassociation

To obtain a single-cell suspension, dissected tumors were enzymatically and mechanically disrupted. First, the tumors were mechanically minced using surgical disposable scalpels (Surgical Design, catalog no. SCALPEL 12B) into pieces smaller than 5 mm in diameter on a 6 cm plate (Falcon, catalog no. 353002). Next, 2 mL of enzymatic cocktail [8 mg of collagenase IV (Gibco, catalog no. 17104-019), 800 µL of dispase (Stem Cell Technologies, catalog no. 07913), and 25 µg of DNase (Sigma Aldrich, catalog no. D4263-5VL) diluted in FBS-free MEM (Corning, catalog no. 10-009-CV)] was added to the minced tumors. The mixture was incubated for 20 minutes at 37°C in a non-CO_2 incubator. Minced tumor pieces were then further disrupted by smashing them between two fully frosted cytology slides (Fisherbrand, catalog no. 1255015). The resulting single-cell suspension was filtered through a 70 µm strainer (Fisherbrand, catalog no. 22-363-548) and resuspended in 5 mL of FBS-free media. The cells were centrifuged at 350 g for 5 minutes at 4°C and resuspended in 1x RBC lysis buffer (BD, catalog no. 555899). The RBC lysis reaction was incubated for 2–5 minutes at room temperature, after which the reaction was stopped by adding 5 mL of FBS-free media. The cells were then centrifuged at 350 g for 5 minutes at 4°C, resuspended in DPBS, and were ready for subsequent procedures.

Single-cell RNA-Sequencing

Yumm5.2 sh*Cdkn2a* hairpins #1 and #2, and control shGFP cells were subcutaneously implanted into five mice per condition, as outlined in the *Mice Models* section. Once reached a volume of 0.5 cm^3, tumors were harvested and processed into a single-cell

suspension as described in the *Tumor cell disassociation* section. Single-cell suspensions were first stained with a 1:4000 dilution of viability dye (ThermoFisher Scientific, catalog no. 65-0863-14) in DPBS for 20 minutes on ice and in the dark. Then, cells were centrifuged at 350 g for 5 minutes at 4°C and stained with 2 µg/mL of anti-CD45 PE-conjugated antibody (ThermoFisher Scientific, catalog no. 12-0451-83), diluted in EasySep™ buffer (Stemcell Technologies, catalog no. 20144) for 20 minutes on ice and protected from light. After centrifugation at 350 g for 5 minutes at 4°C, cells were resuspended and pooled by sample group in 5 mL of FBS-free MEM media (Corning, catalog no. 10-009-CV). Single live PE-positive (Cd45+) cells were sorted using a Sony MA900 cell sorter (serial no. 0714313) and collected in 0.04% BSA/PBS for downstream processing. cDNA Libraries were prepared at the University of Pittsburgh Single Cell Core Facility. Briefly, viability was confirmed with greater than 80% live cells using a Nexcelom automated cell counter (serial no. Auto2000-201-1019). Samples were then labeled with TotalSeq-C antibody hashtags (Biolgened, catalog no. 155881, 155883, 155885, 155887, 155889, 155891) following manufacturer's instructions. Equal numbers of cells from each sample were then pooled together and loaded onto the Chromium controller (serial no. CXVG11091) for single-cell capture and barcoding. cDNA library preparation was carried out using the Chromium Next GEM Single Cell 5' Reagent Kits v2 (10X Genomics, catalog no. PN-1000265) following the manufacturer's protocol. Finally, the indexed libraries were sequenced on an Illumina NovaSeq 6000 platform at the Health Sciences Sequencing Core at UPMC Children's Hospital of Pittsburgh.

The resulting sequencing data were processed using the CellRanger pipeline (10X Genomics, v.2.1.1), which generated cell-gene unique molecular identifier (UMI) count matrices. Further data analysis, including quality control (QC), normalization, and downstream analysis, was performed using the Scanpy package. After QC filtering and normalization, cells were clustered using the Louvain algorithm, which is available as part of the Scanpy package, to identify distinct cell populations based on gene expression patterns. Cell identities were determined by analyzing the top-expressed genes in each cluster, with further identification based on the expression of known cell-type marker genes

Macrophage Profiling

Tumors were harvested and processed into a single-cell suspension as described in the *Tumor cell disassociation* section. Notice that for experiments where phagocytosis was assessed, dTOMATO-expressing cancer cells were implanted. Single-cell suspensions were first blocked with 5 µg/mL of Cd16/Cd32 (Invitrogen, catalog no. 14016185) diluted in DPBS for 10 minutes on ice. Cells were stained for 20 minutes at 4°C protected from the light after which cells were fixed in 4% paraformaldehyde (Sigma Aldrich, catalog no. 158127-3Kg) for 15 minutes at 4°C, shielded from light, and resuspended in FACS buffer (1x PBS, 10 mM HEPES [Gibco, catalog no. 15630080], 1% heat-inactivated FBS [Sigma Aldrich, catalog no. F4135-100ML], 0.05% sodium azide [Sigma Aldrich, catalog no. S2002-25G]). Stained cells were immediately analyzed on a Fortessa (Beckman Coulter, serial no. H64717700020). FlowJo version 10 was used for further analysis. Antibodies and concentrations used in this study include: 0.5 µg/mL of anti-Cd11b Brilliant Violet 421-conjugated antibody (Biolegend, catalog no. 101236), 4 µg/mL of anti-F4/80 APC-

conjugated antibody (Biolegend, catalog no. 123116), 2 µg/mL of anti-PD-1 Brilliant Violet 650-conjugated antibody (Thermofisher Scientific, catalog no. 416-9985-82), 2 µg/mL of anti-PD-L1 PE/Cyanine5-conjugated antibody (Biolgened, catalog no. 124344), 50 µM Zinpyr-1 (Cayman Chemical, catalog no. 15122). Antibodies were diluted in DPBS, containing a 1:1000 dilution of Live/Dead Fixable Near-IR Dead Cell Stain kit (Invitrogen, catalog no. L34976).

In vitro phagocytosis activity

Seventy-five thousand RAW 264.7 cells were seeded in 12-well plates (Corning, catalog no. 3513) containing 1.5 mL of regular media and incubated at 37°C and 5% CO_2. Seventy-two hours later cells were washed with PBS and media replaced for 1.5 mL of 200 µg/mL of pHrodo red E.coli particles (Invitrogen, catalog no. P35361) resuspended in media without FBS and incubated 1h at 37°C and 5% CO_2. Cells were scrapped out and stained with zinpry-1 and Live/Dead Fixable Near-IR Dead Cell Stain as described in *Labile Zinc quantification* section above. Stained cells were immediately analyzed on a Fortessa (Beckman Coulter, serial no. H64717700020). Flow cytometry data were analyzed with FlowJo version 10. The median fluorescence intensity (MFI) of single live cells was measured to assess the labile zinc content and the phagocytic activity per sample.

Patient scRNA-Seq data sets and processing

The Jereby-Arnon 2018 melanoma dataset[178] and the Chen 2020 Head and Neck dataset[179] were downloaded from the Gene Expression Omnibus (GSE115978 and GSE150430, respectively). For sample processing, genes were retained if expressed in

at least three cells, cells were kept if they had more than 200 features, and cells with >20% mitochondrial reads were removed. Library size bias was corrected using Seurat's NormalizeData, scaling expression values to 10,000 counts per cell and log-transforming the data. Data was then scaled using Seurat's ScaleData with all genes as features. Cancer cells and macrophages were annotated based on publicly available cell type labels. Tumor samples were then stratified into *CDKN2A*^{High} and *CDKN2A*^{Low} groups based on *CDKN2A* median expression in the cancer cell compartment. Signature scores were calculated as the mean expression of genes in predefined signatures (**Table S4**) for each cell in the macrophage or cancer cell compartment.

Western Blotting

Cell lysates were collected in 1X sample buffer [2% SDS (Millipore Sigma, catalog no. 75746-1Kg), 10% glycerol (Sigma Aldrich, catalog no. G5516), 0.01% bromophenol blue (Millipore Sigma, catalog no. BX1410), 62.5 mM Tris (Fisher Scientific, catalog no. AAJ65594A1), pH=6.8 and 0.1 M DTT (Thermo Fisher, catalog no. 15508-013)] and boiled at 95° C for 10 minutes. Protein concentration was determined using Bradford assay (Bio-Rad, catalog no. 5000006) following manufacturer's instructions. Proteins were resolved using SDS-PAGE gels and transferred to nitrocellulose membranes (GE Healthcare Life Sciences, catalog no. 10600001) as previously described[4]. Antibodies used include: anti human p16 (Abcam, catalog no. ab108349, working concentration 1.5 µg/mL), mouse anti-p16 (Cell Signaling Technology, catalog no. 29271S, working concentration 1 µg/mL), anti-p19 (Abcam, catalog no. ab80, working concentration 1 µg/mL), anti-β-Actin (Sigma-Aldrich, catalog no. A1978, working concentration 1 µg/mL), anti-

mouse HRP (Cell Signaling Technology, catalog no. 7076, working concentration 0.1 µg/mL), and anti-rabbit HRP (Cell Signaling Technology, catalog no. 7074, , working concentration 0.2 µg/mL).

Bulk RNA-Seq and RT-qPCR

Total RNA was extracted from cells with Trizol (Ambion, catalog no. 15596018) and DNase treated, cleaned, and concentrated using Zymo columns (Zymo Research, catalog no. R1013) following the manufacturer's instructions. Optical density values for RNA were measured using NanoDrop One (Thermo Scientific) to confirm an A260 and A280 ratios above 1.9. For bulk RNA-Seq, RNA integrity number (RIN) was measured using BioAnalyzer (Agilent Technologies; RRID:SCR_019715) RNA 6000 Nano Kit to confirm RIN above 7 for each sample. The cDNA libraries, next-generation sequencing, and bioinformatics analysis was performed by Novogene. Differential expression analysis was done using DESeq (v2_1.6.3). Three technical replicates were used.

For RT-qPCR, a total of 2 µg of RNA was reverse-transcribed to cDNA (Applied Biosystems, catalog no. A25742) following manufacturer's instructions in a thermal cycler (Bio-Rad, T100™ Thermal Cycler, serial no. 621BR59583). Relative expression of target genes was analyzed using the Real-Time PCR System (Bio-Rad, CFX Connect, serial no. 788BR09362) with clear 96-well plates (Greiner Bio-One, catalog no. 652240). Primers were designed using the Integrated DNA Technologies (IDT) web tool (**Table S7**). Conditions for amplification were: 5 min at 95° C, 40 cycles of 10 sec at 95° C and 7 sec at 62° C. The assay ended with a melting curve program: 15 sec at 95° C, 1 min at 70°

C, then ramping to 95° C while continuously monitoring fluorescence. Each sample was assessed in triplicate. Relative quantification was determined to multiple reference genes (Rplp0, Gusb, and Rp132) to ensure reproducibility using the delta-delta CT method.

Senescence and proliferation assays

SA-β-Gal staining was performed as previously described[180]. Cells were fixed in a mixure of 2% formaldehyde (Fisher Scientific, catalog no. BP531-500) and 0.2% glutaraldehyde (Fisher Scientific, catalog no. 01909-100) diluted in PBS for 5 minutes, followed by staining with a staining cocktail containing: 40 mM Na_2HPO_4 (Sigma Aldrich, catalog no. 567547), 150 mM NaCl (Sigma Aldrich, catalog no. S5886), 2 mM $MgCl_2$ (Sigma Aldrich, catalog no. M1028), 5Mm $K_3Fe(CN)_6$ (Sigma Aldrich, catalog no. 244023), 5 mM $K_4Fe(CN)_6$ (Sigma Aldrich, catalog no. 455989), and 1 mg/ml 5-Bromo-4-chloro-3-indolyl β-D-galactopyranoside (Sigma Aldrich, catalog no. B4252). Staining was incubated overnight at 37° C in a non-CO2 incubator after which reaction was stopped with tap water. Images were acquired immediately upon reaction stopped using an inverted microscope (Nikon Eclipse Ts2, serial no. 139045) with a 20X/0.40 objective (Nikon LWD) equipped with a camera (Nikon DS-Fi3). Each sample was assessed in triplicate and at least 100 cells per well were counted (>300 cells per experiment). For colony formation, an equal number of cells were seeded in 12-well plates and cultured for an additional 1-2 weeks. Colony formation was visualized by fixing cells in 1% paraformaldehyde for 5 minutes followed by staining with 0.05% crystal violet for 20 minutes on rocking. Wells were destained in 500mL 10% acetic acid for 10 minutes on rocking and absorbance (590 nm)

measured using a spectrophotometer (Promega GloMax explorer, serial no. 9720100141). Each sample was assessed in triplicate.

Qualification and Statistical analysis

GraphPad Prism version 10.0 was used to perform statistical analysis. The level of significance between two groups was assessed with pared or unpaired Student's *t* test as necessary and indicated in figure caption. For data sets with more than two groups, one-way ANOVA followed by Šidák correction for multiple comparisons was applied. For longitudinal tumor growth studies mixed-effects model was used and Šidák correction for multiple comparisons was applied. For survival analysis log-rank (Mantel-Cox) test was used. P-values <0.05 were considered significant. Pearson correlation was used to assess the correlation. Specific statistical details used in scRNA-Seq and bulk RNA-Seq data are included in the corresponding section.

BIBLIOGRAPHY

1 Zhao, R., Choi, B. Y., Lee, M. H., Bode, A. M. & Dong, Z. Implications of Genetic and Epigenetic Alterations of CDKN2A (p16(INK4a)) in Cancer. *EBioMedicine* **8**, 30-39 (2016). https://doi.org:10.1016/j.ebiom.2016.04.017

2 Kreuger, I. Z. M., Slieker, R. C., van Groningen, T. & van Doorn, R. Therapeutic Strategies for Targeting CDKN2A Loss in Melanoma. *J Invest Dermatol* **143**, 18-25 e11 (2023). https://doi.org:10.1016/j.jid.2022.07.016

3 Sherr, C. J. The INK4a/ARF network in tumour suppression. *Nat Rev Mol Cell Biol* **2**, 731-737 (2001). https://doi.org:10.1038/35096061

4 Buj, R. *et al.* Suppression of p16 Induces mTORC1-Mediated Nucleotide Metabolic Reprogramming. *Cell Rep* **28**, 1971-1980 e1978 (2019). https://doi.org:10.1016/j.celrep.2019.07.084

5 Buj, R., Leon, K. E., Anguelov, M. A. & Aird, K. M. Suppression of p16 alleviates the senescence-associated secretory phenotype. *Aging (Albany NY)* **13**, 3290-3312 (2021). https://doi.org:10.18632/aging.202640

6 Tangudu, N. K. *et al.* De Novo Purine Metabolism is a Metabolic Vulnerability of Cancers with Low p16 Expression. *Cancer Res Commun* **4**, 1174-1188 (2024). https://doi.org:10.1158/2767-9764.Crc-23-0450

7 Tangudu, N. K. *et al.* ATR promotes mTORC1 activation via de novo cholesterol synthesis in p16-low cancer cells. *bioRxiv* (2023). https://doi.org:10.1101/2023.10.27.564195

8 Wolff, B. & Naumann, M. INK4 cell cycle inhibitors direct transcriptional inactivation of NF-kappaB. *Oncogene* **18**, 2663-2666 (1999). https://doi.org:10.1038/sj.onc.1202617

9 Tyagi, E. *et al.* Loss of p16(INK4A) stimulates aberrant mitochondrial biogenesis through a CDK4/Rb-independent pathway. *Oncotarget* **8**, 55848-55862 (2017). https://doi.org:10.18632/oncotarget.19862

10 Jenkins, N. C. *et al.* The p16(INK4A) tumor suppressor regulates cellular oxidative stress. *Oncogene* **30**, 265-274 (2011). https://doi.org:10.1038/onc.2010.419

11 Choi, B. Y. *et al.* The tumor suppressor p16(INK4a) prevents cell transformation through inhibition of c-Jun phosphorylation and AP-1 activity. *Nat Struct Mol Biol* **12**, 699-707 (2005). https://doi.org:10.1038/nsmb960

12 Lee, M. H. *et al.* Tumor suppressor p16(INK4a) inhibits cancer cell growth by downregulating eEF1A2 through a direct interaction. *J Cell Sci* **126**, 1744-1752 (2013). https://doi.org:10.1242/jcs.113613

13 Al-Khalaf, H. H., Mohideen, P., Nallar, S. C., Kalvakolanu, D. V. & Aboussekhra, A. The cyclin-dependent kinase inhibitor p16INK4a physically interacts with transcription factor Sp1 and cyclin-dependent kinase 4 to transactivate microRNA-141 and microRNA-146b-5p spontaneously and in response to ultraviolet light-induced DNA damage. *J Biol Chem* **288**, 35511-35525 (2013). https://doi.org:10.1074/jbc.M113.512640

14 Buj, R. & Aird, K. M. p16: cycling off the beaten path. *Mol Cell Oncol* **6**, e1677140 (2019). https://doi.org:10.1080/23723556.2019.1677140

15 Murakami, Y., Mizoguchi, F., Saito, T., Miyasaka, N. & Kohsaka, H. p16(INK4a) exerts an anti-inflammatory effect through accelerated IRAK1 degradation in

macrophages. *J Immunol* **189**, 5066-5072 (2012). https://doi.org:10.4049/jimmunol.1103156

16 Gutiontov, S. I. *et al.* CDKN2A loss-of-function predicts immunotherapy resistance in non-small cell lung cancer. *Scientific reports* **11**, 20059 (2021). https://doi.org:10.1038/s41598-021-99524-1

17 Han, G. *et al.* 9p21 loss confers a cold tumor immune microenvironment and primary resistance to immune checkpoint therapy. *Nature communications* **12**, 5606 (2021). https://doi.org:10.1038/s41467-021-25894-9

18 Tu, Z. *et al.* The cell senescence regulator p16 is a promising cancer prognostic and immune check-point inhibitor (ICI) therapy biomarker. *Aging (Albany NY)* **15**, 2136-2157 (2023). https://doi.org:10.18632/aging.204601

19 Yu, J. *et al.* Genetic Aberrations in the CDK4 Pathway Are Associated with Innate Resistance to PD-1 Blockade in Chinese Patients with Non-Cutaneous Melanoma. *Clin Cancer Res* **25**, 6511-6523 (2019). https://doi.org:10.1158/1078-0432.CCR-19-0475

20 Adib, E. *et al.* CDKN2A Alterations and Response to Immunotherapy in Solid Tumors. *Clin Cancer Res* **27**, 4025-4035 (2021). https://doi.org:10.1158/1078-0432.CCR-21-0575

21 Chen, Z. *et al.* Comprehensive Analysis Revealed that CDKN2A is a Biomarker for Immune Infiltrates in Multiple Cancers. *Front Cell Dev Biol* **9**, 808208 (2021). https://doi.org:10.3389/fcell.2021.808208

22 Deng, C. *et al.* Pan-cancer analysis of CDKN2A alterations identifies a subset of gastric cancer with a cold tumor immune microenvironment. *Hum Genomics* **18**, 55 (2024). https://doi.org:10.1186/s40246-024-00615-7

23 Fan, K., Dong, Y., Li, T. & Li, Y. Cuproptosis-associated CDKN2A is targeted by plicamycin to regulate the microenvironment in patients with head and neck squamous cell carcinoma. *Front Genet* **13**, 1036408 (2022). https://doi.org:10.3389/fgene.2022.1036408

24 Liu, S. *et al.* Response and recurrence correlates in individuals treated with neoadjuvant anti-PD-1 therapy for resectable oral cavity squamous cell carcinoma. *Cell Rep Med* **2**, 100411 (2021). https://doi.org:10.1016/j.xcrm.2021.100411

25 Luo, J. P., Wang, J. & Huang, J. H. CDKN2A is a prognostic biomarker and correlated with immune infiltrates in hepatocellular carcinoma. *Biosci Rep* **41** (2021). https://doi.org:10.1042/BSR20211103

26 Peng, Y. *et al.* Co-occurrence of CDKN2A/B and IFN-I homozygous deletions correlates with an immunosuppressive phenotype and poor prognosis in lung adenocarcinoma. *Mol Oncol* **16**, 1746-1760 (2022). https://doi.org:10.1002/1878-0261.13206

27 Zhao, L., Zhou, X., Li, H., Yin, T. & Jiang, Y. Prognosis of immunotherapy for non-small cell lung cancer with CDKN2A loss of function. *J Thorac Dis* **16**, 507-515 (2024). https://doi.org:10.21037/jtd-23-1017

28 Leon, K. E., Tangudu, N. K., Aird, K. M. & Buj, R. Loss of p16: A Bouncer of the Immunological Surveillance? *Life (Basel)* **11** (2021). https://doi.org:10.3390/life11040309

29 Banchereau, R. *et al.* Molecular determinants of response to PD-L1 blockade across tumor types. *Nat Commun* **12**, 3969 (2021). https://doi.org:10.1038/s41467-021-24112-w
30 Wang, S. *et al.* Loss of CDKN2A Enhances the Efficacy of Immunotherapy in EGFR Mutant Non-Small Cell Lung Cancer. *Cancer Res* (2024). https://doi.org:10.1158/0008-5472.CAN-24-1817
31 Xue, L. *et al.* Next-generation sequencing identifies CDKN2A alterations as prognostic biomarkers in recurrent or metastatic head and neck squamous cell carcinoma predominantly receiving immune checkpoint inhibitors. *Front Oncol* **13**, 1276009 (2023). https://doi.org:10.3389/fonc.2023.1276009
32 Jang, H. J. *et al.* Inhibition of Cyclin Dependent Kinase 4/6 Overcomes Primary Resistance to Programmed Cell Death 1 Blockade in Malignant Mesothelioma. *Ann Thorac Surg* **114**, 1842-1852 (2022). https://doi.org:10.1016/j.athoracsur.2021.08.054
33 Brahmer, J. R. *et al.* Safety and activity of anti-PD-L1 antibody in patients with advanced cancer. *N Engl J Med* **366**, 2455-2465 (2012). https://doi.org:10.1056/NEJMoa1200694
34 Topalian, S. L. *et al.* Safety, activity, and immune correlates of anti-PD-1 antibody in cancer. *N Engl J Med* **366**, 2443-2454 (2012). https://doi.org:10.1056/NEJMoa1200690
35 Wolchok, J. D. *et al.* Final, 10-Year Outcomes with Nivolumab plus Ipilimumab in Advanced Melanoma. *N Engl J Med* (2024). https://doi.org:10.1056/NEJMoa2407417
36 Finn, R. S. *et al.* Atezolizumab plus Bevacizumab in Unresectable Hepatocellular Carcinoma. *N Engl J Med* **382**, 1894-1905 (2020). https://doi.org:10.1056/NEJMoa1915745
37 Herbst, R. S. *et al.* Atezolizumab for First-Line Treatment of PD-L1-Selected Patients with NSCLC. *N Engl J Med* **383**, 1328-1339 (2020). https://doi.org:10.1056/NEJMoa1917346
38 Pardoll, D. M. The blockade of immune checkpoints in cancer immunotherapy. *Nat Rev Cancer* **12**, 252-264 (2012). https://doi.org:10.1038/nrc3239
39 Gordon, S. R. *et al.* PD-1 expression by tumour-associated macrophages inhibits phagocytosis and tumour immunity. *Nature* **545**, 495-499 (2017). https://doi.org:10.1038/nature22396
40 Wang, F. *et al.* Tumor-derived exosomes induce PD1(+) macrophage population in human gastric cancer that promotes disease progression. *Oncogenesis* **7**, 41 (2018). https://doi.org:10.1038/s41389-018-0049-3
41 Bally, A. P. *et al.* NF-kappaB regulates PD-1 expression in macrophages. *J Immunol* **194**, 4545-4554 (2015). https://doi.org:10.4049/jimmunol.1402550
42 Han, Z. *et al.* Reprogramming of PD-1+ M2-like tumor-associated macrophages with anti-PD-L1 and lenalidomide in cutaneous T cell lymphoma. *JCI Insight* **8** (2023). https://doi.org:10.1172/jci.insight.163518
43 Coulton, A. *et al.* Using a pan-cancer atlas to investigate tumour associated macrophages as regulators of immunotherapy response. *Nat Commun* **15**, 5665 (2024). https://doi.org:10.1038/s41467-024-49885-8

44 Strauss, L. *et al.* Targeted deletion of PD-1 in myeloid cells induces antitumor immunity. *Sci Immunol* **5** (2020). https://doi.org:10.1126/sciimmunol.aay1863
45 Kim, I. S. *et al.* Immuno-subtyping of breast cancer reveals distinct myeloid cell profiles and immunotherapy resistance mechanisms. *Nature cell biology* **21**, 1113-1126 (2019). https://doi.org:10.1038/s41556-019-0373-7
46 Yu, J. *et al.* Liver metastasis restrains immunotherapy efficacy via macrophage-mediated T cell elimination. *Nature medicine* **27**, 152-164 (2021). https://doi.org:10.1038/s41591-020-1131-x
47 Zhang, Y. *et al.* Myeloid cells are required for PD-1/PD-L1 checkpoint activation and the establishment of an immunosuppressive environment in pancreatic cancer. *Gut* **66**, 124-136 (2017). https://doi.org:10.1136/gutjnl-2016-312078
48 Davar, D. *et al.* Neoadjuvant vidutolimod and nivolumab in high-risk resectable melanoma: A prospective phase II trial. *Cancer Cell* **42**, 1898-1918 e1812 (2024). https://doi.org:10.1016/j.ccell.2024.10.007
49 Shen, L. *et al.* PD-1/PD-L pathway inhibits M.tb-specific CD4(+) T-cell functions and phagocytosis of macrophages in active tuberculosis. *Sci Rep* **6**, 38362 (2016). https://doi.org:10.1038/srep38362
50 Wang, L. *et al.* PD-L1-expressing tumor-associated macrophages are immunostimulatory and associate with good clinical outcome in human breast cancer. *Cell Rep Med* **5**, 101420 (2024). https://doi.org:10.1016/j.xcrm.2024.101420
51 Liu, M. *et al.* Metabolic rewiring of macrophages by CpG potentiates clearance of cancer cells and overcomes tumor-expressed CD47-mediated 'don't-eat-me' signal. *Nat Immunol* **20**, 265-275 (2019). https://doi.org:10.1038/s41590-018-0292-y
52 Ring, N. G. *et al.* Anti-SIRPalpha antibody immunotherapy enhances neutrophil and macrophage antitumor activity. *Proc Natl Acad Sci U S A* **114**, E10578-E10585 (2017). https://doi.org:10.1073/pnas.1710877114
53 Gonzalez, M. A. *et al.* Phagocytosis increases an oxidative metabolic and immune suppressive signature in tumor macrophages. *J Exp Med* **220** (2023). https://doi.org:10.1084/jem.20221472
54 Hu, Y. *et al.* Dual roles of hexokinase 2 in shaping microglial function by gating glycolytic flux and mitochondrial activity. *Nat Metab* **4**, 1756-1774 (2022). https://doi.org:10.1038/s42255-022-00707-5
55 Davies, L. C. *et al.* Peritoneal tissue-resident macrophages are metabolically poised to engage microbes using tissue-niche fuels. *Nat Commun* **8**, 2074 (2017). https://doi.org:10.1038/s41467-017-02092-0
56 Kiouri, D. P. *et al.* Multifunctional role of zinc in human health: an update. *EXCLI J* **22**, 809-827 (2023). https://doi.org:10.17179/excli2023-6335
57 Sugimoto, R. *et al.* Zinc Deficiency as a General Feature of Cancer: a Review of the Literature. *Biol Trace Elem Res* **202**, 1937-1947 (2024). https://doi.org:10.1007/s12011-023-03818-6
58 Jeong, J. & Eide, D. J. The SLC39 family of zinc transporters. *Mol Aspects Med* **34**, 612-619 (2013). https://doi.org:10.1016/j.mam.2012.05.011

59 Huang, L. & Tepaamorndech, S. The SLC30 family of zinc transporters - a review of current understanding of their biological and pathophysiological roles. *Mol Aspects Med* **34**, 548-560 (2013). https://doi.org:10.1016/j.mam.2012.05.008
60 Si, M. & Lang, J. The roles of metallothioneins in carcinogenesis. *J Hematol Oncol* **11**, 107 (2018). https://doi.org:10.1186/s13045-018-0645-x
61 Mehta, A. J., Yeligar, S. M., Elon, L., Brown, L. A. & Guidot, D. M. Alcoholism causes alveolar macrophage zinc deficiency and immune dysfunction. *Am J Respir Crit Care Med* **188**, 716-723 (2013). https://doi.org:10.1164/rccm.201301-0061OC
62 Wirth, J. J., Fraker, P. J. & Kierszenbaum, F. Zinc requirement for macrophage function: effect of zinc deficiency on uptake and killing of a protozoan parasite. *Immunology* **68**, 114-119 (1989).
63 Sheikh, A. *et al.* Zinc influences innate immune responses in children with enterotoxigenic Escherichia coli-induced diarrhea. *J Nutr* **140**, 1049-1056 (2010). https://doi.org:10.3945/jn.109.111492
64 Hall, S. C. *et al.* Critical Role of Zinc Transporter (ZIP8) in Myeloid Innate Immune Cell Function and the Host Response against Bacterial Pneumonia. *J Immunol* **207**, 1357-1370 (2021). https://doi.org:10.4049/jimmunol.2001395
65 Kitamura, H. *et al.* Toll-like receptor-mediated regulation of zinc homeostasis influences dendritic cell function. *Nat Immunol* **7**, 971-977 (2006). https://doi.org:10.1038/ni1373
66 Mocchegiani, E. *et al.* Metallothioneins/PARP-1/IL-6 interplay on natural killer cell activity in elderly: parallelism with nonagenarians and old infected humans. Effect of zinc supply. *Mech Ageing Dev* **124**, 459-468 (2003). https://doi.org:10.1016/s0047-6374(03)00023-x
67 Aydemir, T. B., Blanchard, R. K. & Cousins, R. J. Zinc supplementation of young men alters metallothionein, zinc transporter, and cytokine gene expression in leukocyte populations. *Proceedings of the National Academy of Sciences of the United States of America* **103**, 1699-1704 (2006). https://doi.org:10.1073/pnas.0510407103
68 Shi, H. N., Scott, M. E., Stevenson, M. M. & Koski, K. G. Energy restriction and zinc deficiency impair the functions of murine T cells and antigen-presenting cells during gastrointestinal nematode infection. *J Nutr* **128**, 20-27 (1998). https://doi.org:10.1093/jn/128.1.20
69 Ren, X. *et al.* SLC39A10 promotes malignant phenotypes of gastric cancer cells by activating the CK2-mediated MAPK/ERK and PI3K/AKT pathways. *Exp Mol Med* **55**, 1757-1769 (2023). https://doi.org:10.1038/s12276-023-01062-5
70 Li, M. *et al.* Aberrant expression of zinc transporter ZIP4 (SLC39A4) significantly contributes to human pancreatic cancer pathogenesis and progression. *Proc Natl Acad Sci U S A* **104**, 18636-18641 (2007). https://doi.org:10.1073/pnas.0709307104
71 Cheng, X. *et al.* Zinc transporter SLC39A13/ZIP13 facilitates the metastasis of human ovarian cancer cells via activating Src/FAK signaling pathway. *J Exp Clin Cancer Res* **40**, 199 (2021). https://doi.org:10.1186/s13046-021-01999-3
72 Hogstrand, C., Kille, P., Ackland, M. L., Hiscox, S. & Taylor, K. M. A mechanism for epithelial-mesenchymal transition and anoikis resistance in breast cancer triggered by zinc channel ZIP6 and STAT3 (signal transducer and activator of

transcription 3). *Biochem J* **455**, 229-237 (2013). https://doi.org:10.1042/BJ20130483

73 Cheng, X. *et al.* Solute Carrier Family 39 Member 6 Gene Promotes Aggressiveness of Esophageal Carcinoma Cells by Increasing Intracellular Levels of Zinc, Activating Phosphatidylinositol 3-Kinase Signaling, and Up-regulating Genes That Regulate Metastasis. *Gastroenterology* **152**, 1985-1997 e1912 (2017). https://doi.org:10.1053/j.gastro.2017.02.006

74 Liu, M. *et al.* ZIP4 Promotes Pancreatic Cancer Progression by Repressing ZO-1 and Claudin-1 through a ZEB1-Dependent Transcriptional Mechanism. *Clin Cancer Res* **24**, 3186-3196 (2018). https://doi.org:10.1158/1078-0432.CCR-18-0263

75 Thomas, P., Pang, Y. & Dong, J. Ligand-independent signaling and migration of breast cancer cells expressing membrane androgen receptor, ZIP9 (SLC39A9). *Mol Cell Endocrinol* **578**, 112060 (2023). https://doi.org:10.1016/j.mce.2023.112060

76 Prasad, A. S. *et al.* Nutritional and zinc status of head and neck cancer patients: an interpretive review. *J Am Coll Nutr* **17**, 409-418 (1998). https://doi.org:10.1080/07315724.1998.10718787

77 Federico, A. *et al.* Effects of selenium and zinc supplementation on nutritional status in patients with cancer of digestive tract. *Eur J Clin Nutr* **55**, 293-297 (2001). https://doi.org:10.1038/sj.ejcn.1601157

78 Xie, Y. *et al.* Higher serum zinc levels may reduce the risk of cervical cancer in Asian women: A meta-analysis. *J Int Med Res* **46**, 4898-4906 (2018). https://doi.org:10.1177/0300060518805600

79 Lin, S. & Yang, H. Ovarian cancer risk according to circulating zinc and copper concentrations: A meta-analysis and Mendelian randomization study. *Clin Nutr* **40**, 2464-2468 (2021). https://doi.org:10.1016/j.clnu.2020.10.011

80 Wu, X., Wu, H., Liu, L., Qiang, G. & Zhu, J. Serum zinc level and tissue ZIP4 expression are related to the prognosis of patients with stages I-III colon cancer. *Transl Cancer Res* **9**, 5585-5594 (2020). https://doi.org:10.21037/tcr-20-2571

81 Zhao, J. *et al.* Comparative study of serum zinc concentrations in benign and malignant prostate disease: A Systematic Review and Meta-Analysis. *Sci Rep* **6**, 25778 (2016). https://doi.org:10.1038/srep25778

82 Singh, K. P. *et al.* Effect of zinc on immune functions and host resistance against infection and tumor challenge. *Immunopharmacol Immunotoxicol* **14**, 813-840 (1992). https://doi.org:10.3109/08923979209009237

83 Satoh, M. *et al.* Prevention of carcinogenicity of anticancer drugs by metallothionein induction. *Cancer Res* **53**, 4767-4768 (1993).

84 Sun, J. *et al.* Reduction in squamous cell carcinomas in mouse skin by dietary zinc supplementation. *Cancer Med* **5**, 2032-2042 (2016). https://doi.org:10.1002/cam4.768

85 Fong, L. Y., Mancini, R., Nakagawa, H., Rustgi, A. K. & Huebner, K. Combined cyclin D1 overexpression and zinc deficiency disrupts cell cycle and accelerates mouse forestomach carcinogenesis. *Cancer Res* **63**, 4244-4252 (2003).

86 Tang, W. *et al.* Efficacy of zinc carnosine in the treatment of colorectal cancer and its potential in combination with immunotherapy in vivo. *Aging (Albany NY)* **14**, 8688-8699 (2022). https://doi.org:10.18632/aging.204380
87 Ying Yang, H. F., Xinyu Xu, Shankun Yao, Wenhao Yu and Zijian Guo. Zinc Ion-Induced Immune Responses in Antitumor Immunotherapy. *CCS Chemistry* **0**, 1-20 (2024). https://doi.org:10.31635/ccschem.023.202303514
88 Sugandha Narayan, R. D., Zaigham Abbas Rizvi, Amit Awasthi. Zinc dampens anti-tumor immunity by promoting Foxp3+ regulatory T cells. *Front Immunol* **15** (2024). https://doi.org:10.3389/fimmu.2024.1389387
89 Chang, W., Li, H., Ou, W. & Wang, S. Y. A novel zinc metabolism-related gene signature to predict prognosis and immunotherapy response in lung adenocarcinoma. *Front Immunol* **14**, 1147528 (2023). https://doi.org:10.3389/fimmu.2023.1147528
90 Lim, B., Kim, K. S. & Na, K. pH-Responsive Zinc Ion Regulating Immunomodulatory Nanoparticles for Effective Cancer Immunotherapy. *Biomacromolecules* **24**, 4263-4273 (2023). https://doi.org:10.1021/acs.biomac.3c00557
91 Deleye, Y. *et al.* CDKN2A/p16INK4a suppresses hepatic fatty acid oxidation through the AMPKalpha2-SIRT1-PPARalpha signaling pathway. *J Biol Chem* **295**, 17310-17322 (2020). https://doi.org:10.1074/jbc.RA120.012543
92 Bantubungi, K. *et al.* Cdkn2a/p16Ink4a regulates fasting-induced hepatic gluconeogenesis through the PKA-CREB-PGC1alpha pathway. *Diabetes* **63**, 3199-3209 (2014). https://doi.org:10.2337/db13-1921
93 Bian, Y. *et al.* Cancer SLC43A2 alters T cell methionine metabolism and histone methylation. *Nature* **585**, 277-282 (2020). https://doi.org:10.1038/s41586-020-2682-1
94 Ho, P. C. *et al.* Phosphoenolpyruvate Is a Metabolic Checkpoint of Anti-tumor T Cell Responses. *Cell* **162**, 1217-1228 (2015). https://doi.org:10.1016/j.cell.2015.08.012
95 Chang, C. H. *et al.* Metabolic Competition in the Tumor Microenvironment Is a Driver of Cancer Progression. *Cell* **162**, 1229-1241 (2015). https://doi.org:10.1016/j.cell.2015.08.016
96 Li, Z. *et al.* SLC3A2 promotes tumor-associated macrophage polarization through metabolic reprogramming in lung cancer. *Cancer Sci* **114**, 2306-2317 (2023). https://doi.org:10.1111/cas.15760
97 Sage, M. A. G. & Duffy, D. M. Novel Plasma Membrane Androgen Receptor SLC39A9 Mediates Ovulatory Changes in Cells of the Monkey Ovarian Follicle. *Endocrinology* **165** (2024). https://doi.org:10.1210/endocr/bqae071
98 Converse, A. & Thomas, P. The zinc transporter ZIP9 (Slc39a9) regulates zinc dynamics essential to egg activation in zebrafish. *Sci Rep* **10**, 15673 (2020). https://doi.org:10.1038/s41598-020-72515-4
99 Thomas, P. & Dong, J. (-)-Epicatechin acts as a potent agonist of the membrane androgen receptor, ZIP9 (SLC39A9), to promote apoptosis of breast and prostate cancer cells. *The Journal of steroid biochemistry and molecular biology* **211**, 105906 (2021). https://doi.org:10.1016/j.jsbmb.2021.105906

100 Thomas, P., Pang, Y. & Dong, J. Membrane androgen receptor characteristics of human ZIP9 (SLC39A) zinc transporter in prostate cancer cells: Androgen-specific activation and involvement of an inhibitory G protein in zinc and MAP kinase signaling. *Mol Cell Endocrinol* **447**, 23-34 (2017). https://doi.org:10.1016/j.mce.2017.02.025
101 Matsuura, W. *et al.* SLC39A9 (ZIP9) regulates zinc homeostasis in the secretory pathway: characterization of the ZIP subfamily I protein in vertebrate cells. *Biosci Biotechnol Biochem* **73**, 1142-1148 (2009). https://doi.org:10.1271/bbb.80910
102 Yamaji, T. *et al.* A CRISPR Screen Using Subtilase Cytotoxin Identifies SLC39A9 as a Glycan-Regulating Factor. *iScience* **15**, 407-420 (2019). https://doi.org:10.1016/j.isci.2019.05.005
103 Zhang, T. *et al.* Crystal structures of a ZIP zinc transporter reveal a binuclear metal center in the transport pathway. *Sci Adv* **3**, e1700344 (2017). https://doi.org:10.1126/sciadv.1700344
104 Bulldan, A., Malviya, V. N., Upmanyu, N., Konrad, L. & Scheiner-Bobis, G. Testosterone/bicalutamide antagonism at the predicted extracellular androgen binding site of ZIP9. *Biochim Biophys Acta Mol Cell Res* **1864**, 2402-2414 (2017). https://doi.org:10.1016/j.bbamcr.2017.09.012
105 Bukiya, A. N. & Dopico, A. M. Common structural features of cholesterol binding sites in crystallized soluble proteins. *J Lipid Res* **58**, 1044-1054 (2017). https://doi.org:10.1194/jlr.R073452
106 Tumeh, P. C. *et al.* PD-1 blockade induces responses by inhibiting adaptive immune resistance. *Nature* **515**, 568-571 (2014). https://doi.org:10.1038/nature13954
107 Cristescu, R. *et al.* Pan-tumor genomic biomarkers for PD-1 checkpoint blockade-based immunotherapy. *Science* **362** (2018). https://doi.org:10.1126/science.aar3593
108 Yang, M., McKay, D., Pollard, J. W. & Lewis, C. E. Diverse Functions of Macrophages in Different Tumor Microenvironments. *Cancer Res* **78**, 5492-5503 (2018). https://doi.org:10.1158/0008-5472.CAN-18-1367
109 Chen, J. J. *et al.* Tumor-associated macrophages: the double-edged sword in cancer progression. *J Clin Oncol* **23**, 953-964 (2005). https://doi.org:10.1200/JCO.2005.12.172
110 Gabrilovich, D. I., Ostrand-Rosenberg, S. & Bronte, V. Coordinated regulation of myeloid cells by tumours. *Nat Rev Immunol* **12**, 253-268 (2012). https://doi.org:10.1038/nri3175
111 Arlauckas, S. P. *et al.* In vivo imaging reveals a tumor-associated macrophage-mediated resistance pathway in anti-PD-1 therapy. *Sci Transl Med* **9** (2017). https://doi.org:10.1126/scitranslmed.aal3604
112 Chow, A. *et al.* Tim-4(+) cavity-resident macrophages impair anti-tumor CD8(+) T cell immunity. *Cancer Cell* **39**, 973-988 e979 (2021). https://doi.org:10.1016/j.ccell.2021.05.006
113 House, I. G. *et al.* Macrophage-Derived CXCL9 and CXCL10 Are Required for Antitumor Immune Responses Following Immune Checkpoint Blockade. *Clin Cancer Res* **26**, 487-504 (2020). https://doi.org:10.1158/1078-0432.CCR-19-1868

114 Serrano, M., Hannon, G. J. & Beach, D. A new regulatory motif in cell-cycle control causing specific inhibition of cyclin D/CDK4. *Nature* **366**, 704-707 (1993). https://doi.org:10.1038/366704a0 [doi]
115 Xiong, Y., Zhang, H. & Beach, D. Subunit rearrangement of the cyclin-dependent kinases is associated with cellular transformation. *Genes Dev* **7**, 1572-1583 (1993). https://doi.org:10.1101/gad.7.8.1572
116 Barriga, F. M. *et al.* MACHETE identifies interferon-encompassing chromosome 9p21.3 deletions as mediators of immune evasion and metastasis. *Nat Cancer* **3**, 1367-1385 (2022). https://doi.org:10.1038/s43018-022-00443-5
117 Newcomer, K. *et al.* Malignant melanoma: evolving practice management in an era of increasingly effective systemic therapies. *Curr Probl Surg* **59**, 101030 (2022). https://doi.org:10.1016/j.cpsurg.2021.101030
118 Clinton, L. K. *et al.* The LAST guidelines in clinical practice: implementing recommendations for p16 use. *Am J Clin Pathol* **144**, 844-849 (2015). https://doi.org:10.1309/AJCPUXLP7XD8OQYY
119 Chan, S. H., Chiang, J. & Ngeow, J. CDKN2A germline alterations and the relevance of genotype-phenotype associations in cancer predisposition. *Hered Cancer Clin Pract* **19**, 21 (2021). https://doi.org:10.1186/s13053-021-00178-x
120 Fraker, P. J. & King, L. E. Reprogramming of the immune system during zinc deficiency. *Annu Rev Nutr* **24**, 277-298 (2004). https://doi.org:10.1146/annurev.nutr.24.012003.132454
121 Costello, L. C. & Franklin, R. B. Cytotoxic/tumor suppressor role of zinc for the treatment of cancer: an enigma and an opportunity. *Expert Rev Anticancer Ther* **12**, 121-128 (2012). https://doi.org:10.1586/era.11.190
122 Mao, W. *et al.* Statin shapes inflamed tumor microenvironment and enhances immune checkpoint blockade in non-small cell lung cancer. *JCI Insight* **7** (2022). https://doi.org:10.1172/jci.insight.161940
123 Cantini, L. *et al.* High-intensity statins are associated with improved clinical activity of PD-1 inhibitors in malignant pleural mesothelioma and advanced non-small cell lung cancer patients. *Eur J Cancer* **144**, 41-48 (2021). https://doi.org:10.1016/j.ejca.2020.10.031
124 Cortellini, A. *et al.* Integrated analysis of concomitant medications and oncological outcomes from PD-1/PD-L1 checkpoint inhibitors in clinical practice. *J Immunother Cancer* **8** (2020). https://doi.org:10.1136/jitc-2020-001361
125 Kansal, V. *et al.* Statin drugs enhance responses to immune checkpoint blockade in head and neck cancer models. *J Immunother Cancer* **11** (2023). https://doi.org:10.1136/jitc-2022-005940
126 Takada, K. *et al.* A propensity score-matched analysis of the impact of statin therapy on the outcomes of patients with non-small-cell lung cancer receiving anti-PD-1 monotherapy: a multicenter retrospective study. *BMC Cancer* **22**, 503 (2022). https://doi.org:10.1186/s12885-022-09385-8
127 Liao, Y., Lin, Y., Ye, X. & Shen, J. Concomitant Statin Use and Survival in Patients With Cancer on Immune Checkpoint Inhibitors: A Meta-Analysis. *JCO Oncol Pract*, OP2400583 (2025). https://doi.org:10.1200/OP-24-00583

128 Wu, J. Y. *et al.* Cancer-Derived Succinate Promotes Macrophage Polarization and Cancer Metastasis via Succinate Receptor. *Mol Cell* **77**, 213-227 e215 (2020). https://doi.org:10.1016/j.molcel.2019.10.023
129 Reinfeld, B. I. *et al.* Cell-programmed nutrient partitioning in the tumour microenvironment. *Nature* **593**, 282-288 (2021). https://doi.org:10.1038/s41586-021-03442-1
130 Epstein, M. M. *et al.* Dietary zinc and prostate cancer survival in a Swedish cohort. *Am J Clin Nutr* **93**, 586-593 (2011). https://doi.org:10.3945/ajcn.110.004804
131 Gonzalez, A., Peters, U., Lampe, J. W. & White, E. Zinc intake from supplements and diet and prostate cancer. *Nutr Cancer* **61**, 206-215 (2009). https://doi.org:10.1080/01635580802419749
132 Li, L. & Gai, X. The association between dietary zinc intake and risk of pancreatic cancer: a meta-analysis. *Biosci Rep* **37** (2017). https://doi.org:10.1042/BSR20170155
133 Pan, S. Y. *et al.* Antioxidants and breast cancer risk- a population-based case-control study in Canada. *BMC Cancer* **11**, 372 (2011). https://doi.org:10.1186/1471-2407-11-372
134 Adzersen, K. H., Jess, P., Freivogel, K. W., Gerhard, I. & Bastert, G. Raw and cooked vegetables, fruits, selected micronutrients, and breast cancer risk: a case-control study in Germany. *Nutr Cancer* **46**, 131-137 (2003). https://doi.org:10.1207/S15327914NC4602_05
135 Lin, L. C. *et al.* Effects of zinc supplementation on clinical outcomes in patients receiving radiotherapy for head and neck cancers: a double-blinded randomized study. *Int J Radiat Oncol Biol Phys* **70**, 368-373 (2008). https://doi.org:10.1016/j.ijrobp.2007.06.073
136 Shi, Z. *et al.* Association between dietary zinc intake and mortality among Chinese adults: findings from 10-year follow-up in the Jiangsu Nutrition Study. *Eur J Nutr* **57**, 2839-2846 (2018). https://doi.org:10.1007/s00394-017-1551-7
137 Gutierrez-Gonzalez, E. *et al.* Dietary Zinc and Risk of Prostate Cancer in Spain: MCC-Spain Study. *Nutrients* **11** (2018). https://doi.org:10.3390/nu11010018
138 Zhang, Y., Song, M., Mucci, L. A. & Giovannucci, E. L. Zinc supplement use and risk of aggressive prostate cancer: a 30-year follow-up study. *Eur J Epidemiol* **37**, 1251-1260 (2022). https://doi.org:10.1007/s10654-022-00922-0
139 Gallus, S. *et al.* Dietary zinc and prostate cancer risk: a case-control study from Italy. *Eur Urol* **52**, 1052-1056 (2007). https://doi.org:10.1016/j.eururo.2007.01.094
140 Fernandez-Lazaro, C. I. *et al.* Dietary Antioxidant Vitamins and Minerals and Breast Cancer Risk: Prospective Results from the SUN Cohort. *Antioxidants (Basel)* **10** (2021). https://doi.org:10.3390/antiox10030340
141 Luo, H. *et al.* Association between Dietary Zinc and Selenium Intake, Oxidative Stress-Related Gene Polymorphism, and Colorectal Cancer Risk in Chinese Population - A Case-Control Study. *Nutr Cancer* **73**, 1621-1630 (2021). https://doi.org:10.1080/01635581.2020.1804950
142 Bravi, F. *et al.* Dietary intake of selected micronutrients and the risk of pancreatic cancer: an Italian case-control study. *Ann Oncol* **22**, 202-206 (2011). https://doi.org:10.1093/annonc/mdq302

143 Hoppe, C. *et al.* Zinc as a complementary treatment for cancer patients: a systematic review. *Clin Exp Med* **21**, 297-313 (2021). https://doi.org:10.1007/s10238-020-00677-6
144 Trumbo, P., Yates, A. A., Schlicker, S. & Poos, M. Dietary reference intakes: vitamin A, vitamin K, arsenic, boron, chromium, copper, iodine, iron, manganese, molybdenum, nickel, silicon, vanadium, and zinc. *J Am Diet Assoc* **101**, 294-301 (2001). https://doi.org:10.1016/S0002-8223(01)00078-5
145 Wang, K. *et al.* Zinc ions activate AKT and promote prostate cancer cell proliferation via disrupting AKT intramolecular interaction. *Oncogene* **44**, 8-18 (2025). https://doi.org:10.1038/s41388-024-03195-x
146 Taylor, K. M. *et al.* ZIP7-mediated intracellular zinc transport contributes to aberrant growth factor signaling in antihormone-resistant breast cancer Cells. *Endocrinology* **149**, 4912-4920 (2008). https://doi.org:10.1210/en.2008-0351
147 Lelliott, E. J. *et al.* Intracellular zinc protects tumours from T cell-mediated cytotoxicity. *Cell Death Differ* **31**, 1707-1716 (2024). https://doi.org:10.1038/s41418-024-01369-4
148 Provinciali, M., Pierpaoli, E., Bartozzi, B. & Bernardini, G. Zinc Induces Apoptosis of Human Melanoma Cells, Increasing Reactive Oxygen Species, p53 and FAS Ligand. *Anticancer Res* **35**, 5309-5316 (2015).
149 Xu, M. *et al.* Zinc-based radioenhancers to activate tumor radioimmunotherapy by PD-L1 and cGAS-STING pathway. *J Nanobiotechnology* **22**, 782 (2024). https://doi.org:10.1186/s12951-024-02999-z
150 Du, M. & Chen, Z. J. DNA-induced liquid phase condensation of cGAS activates innate immune signaling. *Science* **361**, 704-709 (2018). https://doi.org:10.1126/science.aat1022
151 Zhang, L. *et al.* A Peritumorally Injected Immunomodulating Adjuvant Elicits Robust and Safe Metalloimmunotherapy against Solid Tumors. *Adv Mater* **34**, e2206915 (2022). https://doi.org:10.1002/adma.202206915
152 Sies, H. & Jones, D. P. Reactive oxygen species (ROS) as pleiotropic physiological signalling agents. *Nat Rev Mol Cell Biol* **21**, 363-383 (2020). https://doi.org:10.1038/s41580-020-0230-3
153 Kyritsi, K. *et al.* Downregulation of p16 Decreases Biliary Damage and Liver Fibrosis in the Mdr2(/) Mouse Model of Primary Sclerosing Cholangitis. *Gene Expr* **20**, 89-103 (2020). https://doi.org:10.3727/105221620X15889714507961
154 Cudejko, C. *et al.* p16INK4a deficiency promotes IL-4-induced polarization and inhibits proinflammatory signaling in macrophages. *Blood* **118**, 2556-2566 (2011). https://doi.org:10.1182/blood-2010-10-313106
155 Fuentes, L. *et al.* Downregulation of the tumour suppressor p16INK4A contributes to the polarisation of human macrophages toward an adipose tissue macrophage (ATM)-like phenotype. *Diabetologia* **54**, 3150-3156 (2011). https://doi.org:10.1007/s00125-011-2324-0
156 Liang, Y. *et al.* p16(INK4a) Plays Critical Role in Exacerbating Inflammaging in High Fat Diet Induced Skin. *Oxid Med Cell Longev* **2022**, 3415528 (2022). https://doi.org:10.1155/2022/3415528

157 Che, H. *et al.* p16 deficiency attenuates intervertebral disc degeneration by adjusting oxidative stress and nucleus pulposus cell cycle. *eLife* **9** (2020). https://doi.org:10.7554/eLife.52570
158 Zhu, Z., Song, H. & Xu, J. CDKN2A Deletion in Melanoma Excludes T Cell Infiltration by Repressing Chemokine Expression in a Cell Cycle-Dependent Manner. *Front Oncol* **11**, 641077 (2021). https://doi.org:10.3389/fonc.2021.641077
159 Balli, D., Rech, A. J., Stanger, B. Z. & Vonderheide, R. H. Immune Cytolytic Activity Stratifies Molecular Subsets of Human Pancreatic Cancer. *Clin Cancer Res* **23**, 3129-3138 (2017). https://doi.org:10.1158/1078-0432.CCR-16-2128
160 Wartenberg, M. *et al.* Integrated Genomic and Immunophenotypic Classification of Pancreatic Cancer Reveals Three Distinct Subtypes with Prognostic/Predictive Significance. *Clin Cancer Res* **24**, 4444-4454 (2018). https://doi.org:10.1158/1078-0432.CCR-17-3401
161 Morrison, C. *et al.* Predicting response to checkpoint inhibitors in melanoma beyond PD-L1 and mutational burden. *J Immunother Cancer* **6**, 32 (2018). https://doi.org:10.1186/s40425-018-0344-8
162 Nowak, J. E., Harmon, K., Caldwell, C. C. & Wong, H. R. Prophylactic zinc supplementation reduces bacterial load and improves survival in a murine model of sepsis. *Pediatr Crit Care Med* **13**, e323-329 (2012). https://doi.org:10.1097/PCC.0b013e31824fbd90
163 Brazao, V. *et al.* Zinc supplementation increases resistance to experimental infection by Trypanosoma cruzi. *Vet Parasitol* **154**, 32-37 (2008). https://doi.org:10.1016/j.vetpar.2008.02.015
164 Humphrey, P. A., Ashraf, M. & Lee, C. M. Hepatic cells' mitotic and peritoneal macrophage phagocytic activities during Trypanosoma musculi infection in zinc-deficient mice. *J Natl Med Assoc* **89**, 259-267 (1997).
165 Salvin, S. B., Horecker, B. L., Pan, L. X. & Rabin, B. S. The effect of dietary zinc and prothymosin alpha on cellular immune responses of RF/J mice. *Clin Immunol Immunopathol* **43**, 281-288 (1987). https://doi.org:10.1016/0090-1229(87)90137-1
166 Gide, T. N. *et al.* Distinct Immune Cell Populations Define Response to Anti-PD-1 Monotherapy and Anti-PD-1/Anti-CTLA-4 Combined Therapy. *Cancer Cell* **35**, 238-255 e236 (2019). https://doi.org:10.1016/j.ccell.2019.01.003
167 Riaz, N. *et al.* Tumor and Microenvironment Evolution during Immunotherapy with Nivolumab. *Cell* **171**, 934-949 e916 (2017). https://doi.org:10.1016/j.cell.2017.09.028
168 Lee, J. H. *et al.* Transcriptional downregulation of MHC class I and melanoma de-differentiation in resistance to PD-1 inhibition. *Nat Commun* **11**, 1897 (2020). https://doi.org:10.1038/s41467-020-15726-7
169 Hugo, W. *et al.* Genomic and Transcriptomic Features of Response to Anti-PD-1 Therapy in Metastatic Melanoma. *Cell* **165**, 35-44 (2016). https://doi.org:10.1016/j.cell.2016.02.065
170 Gyorffy, B. Integrated analysis of public datasets for the discovery and validation of survival-associated genes in solid tumors. *Innovation (Camb)* **5**, 100625 (2024). https://doi.org:10.1016/j.xinn.2024.100625

171 Gyorffy, B. Transcriptome-level discovery of survival-associated biomarkers and therapy targets in non-small-cell lung cancer. *Br J Pharmacol* **181**, 362-374 (2024). https://doi.org:10.1111/bph.16257
172 Kovacs, S. A., Fekete, J. T. & Gyorffy, B. Predictive biomarkers of immunotherapy response with pharmacological applications in solid tumors. *Acta Pharmacol Sin* **44**, 1879-1889 (2023). https://doi.org:10.1038/s41401-023-01079-6
173 Uphoff, C. C. & Drexler, H. G. Detection of mycoplasma contaminations. *Methods Mol Biol* **290**, 13-23 (2005). https://doi.org:10.1385/1-59259-838-2:013
174 Corrin A. Wohlhieter *et al.* An optimized NGS sample preparation protocol for in vitro CRISPR screens. *STAR Protocols* **2**, 100390 (2021). https://doi.org:10.1016/j.xpro.2021.100390
175 Sullivan, M. R. *et al.* Quantification of microenvironmental metabolites in murine cancers reveals determinants of tumor nutrient availability. *Elife* **8** (2019). https://doi.org:10.7554/eLife.44235
176 Alker, W., Schwerdtle, T., Schomburg, L. & Haase, H. A Zinpyr-1-based Fluorimetric Microassay for Free Zinc in Human Serum. *Int J Mol Sci* **20** (2019). https://doi.org:10.3390/ijms20164006
177 Stringer, C., Wang, T., Michaelos, M. & Pachitariu, M. Cellpose: a generalist algorithm for cellular segmentation. *Nat Methods* **18**, 100-106 (2021). https://doi.org:10.1038/s41592-020-01018-x
178 Jerby-Arnon, L. *et al.* A Cancer Cell Program Promotes T Cell Exclusion and Resistance to Checkpoint Blockade. *Cell* **175**, 984-997 e924 (2018). https://doi.org:10.1016/j.cell.2018.09.006
179 Chen, Y. P. *et al.* Single-cell transcriptomics reveals regulators underlying immune cell diversity and immune subtypes associated with prognosis in nasopharyngeal carcinoma. *Cell Res* **30**, 1024-1042 (2020). https://doi.org:10.1038/s41422-020-0374-x
180 Dimri, G. P. *et al.* A biomarker that identifies senescent human cells in culture and in aging skin in vivo. *Proc Natl Acad Sci U S A* **92**, 9363-9367 (1995). https://doi.org:10.1073/pnas.92.20.9363